

Experimental demonstration of dynamic demand response scheduling for PEM-electrolyzers

Roger Keller^{a,*}, Florian Joseph Baader^b, André Bardow^b, Martin Müller^a, Ralf Peters^{a,c}

^a Forschungszentrum Jülich GmbH, Institute of Energy Technologies (IET), IET-4: Electrochemical Process Engineering, 52425 Jülich, Germany

^b Energy & Process Systems Engineering, Department of Mechanical and Process Engineering, ETH Zürich, Zürich, Switzerland

^c Ruhr University Bochum, Chair of Process Engineering for Synthetic Fuels, Bochum, Germany

HIGHLIGHTS

- Enhanced economic viability of PEM electrolyzers under fluctuating electricity market conditions.
- Experimental validation of real-time scheduling optimization for transient operation in PEM electrolyzers.
- Improved cost efficiency and scalability of 2 MW industrial-scale PEM electrolyzers through simulation-based evaluation.
- Discussion on potential degradation effects induced by overload and temperature conditions, and their implications on the dynamic ramping method.

ARTICLE INFO

Keywords:

PEM electrolyzer
Dynamic ramping constraints
Economic scheduling optimization
Dynamic temperature modelling
Model based feedforward control

ABSTRACT

The use of renewable energy sources, such as wind power and photovoltaics is expected to produce fluctuating electricity prices. These fluctuations give PEM electrolyzers the opportunity to reduce costs, as they can adapt their production rates rapidly. Moreover, typically slow temperature dynamics of electrolyzers increase their flexibility for effective operational management strategies. With a defined temperature trajectory during scheduling optimization, overload operation of the electrolyzer for a given amount of time is possible. However, the temperature dynamics are typically nonlinear. In conjunction with discrete on/off decisions, temperature dynamics lead to mixed-integer nonlinear optimization problems for scheduling that are highly challenging to solve in real time. In this study, we experimentally validate the dynamic ramping scheduling optimization method that precisely linearizes nonlinear temperature dynamics using a flatness-based coordinate transformation. Utilizing the available information from the dynamic scheduling optimization a 100 kW PEM electrolyzer was operated by studying three stack temperature control methods, rejecting disturbances from load variations. Identifying a suitable control method was essential to guarantee the desired temperature tracking performance of the optimization. Our experiments show a 3.8 % cost reduction compared to the benchmark without overload operation. The designed PEM electrolyzer model also deviated only 0.6 % in costs from the experiment. Simulative scaling of PEM electrolysis to 2 MW demonstrates even higher cost reductions with the dynamic ramping method, as the larger electrolyzer has slower dynamics.

1. Introduction

The use of renewable energy sources, such as photovoltaic and wind power, is continuously increasing. As the existing amount of renewable energy in the grid often fluctuates due to weather conditions and its unavailability on demand, the market prices for electrical power

also vary. For “Power to Gas” (PtG) applications producing hydrogen through electrolysis, this creates an opportunity to reduce production costs.

In low-temperature hydrogen electrolysis, two fundamental methods are distinguished, namely: alkaline and proton exchange membrane (PEM) electrolysis. Alkaline electrolysis is already used on a large

* Corresponding author.

Email address: r.keller@fz-juelich.de (R. Keller).

Nomenclature**Abbreviations**

MILP	Mixed-integer linear program
MINLP	Mixed-integer nonlinear program
MPC	Model predictive control
PID	Proportional–Integral–Derivative
PEM	Proton exchange membrane
PtG	Power to gas
PWA	Piece-wise affine

Greek symbols

α	Charge transfer coefficient
η_{act}	Activation losses

Latin symbols

A	Area
C	Heat capacity
c	Concentration
D	Drag factor
F	Faraday constant
ΔG^0	Gibbs energy
ΔH_{HHV}	Higher heating value
j	Current
j_0	Exchange current density
\dot{n}	Molar flow
M	Molar mass
N_{cell}	Number of cells
P	Power
p	Pressure
pr	Price
\dot{Q}	Heat flow

R	Resistance
R_{gas}	Gas constant
T	Temperature
t	Time
τ	Time
U	Voltage
z	Binary variable

Subscripts

0	Initial
A	Anode
con	Contact
el	Electric
f	Final
HT	Heat transfer
K	Cathode
mem	Membrane
ohm	Ohmic
on	On/off-decision
ref	Reference
satt	Saturation
surr	Surroundings

Superscripts

act	Activation
H_2	Hydrogen
max	Maximum
nom	Nominal
O_2	Oxygen
SP	Set-point
steady	Steady state

scale for industrial hydrogen production but is limited by its static load operational behavior [1,2]. PEM electrolysis has the capability of responding to rapid load changes [3,4] and meeting the increasing demand for hydrogen in highly dynamic energy systems dominated by renewable energy sources. These PEM-electrolyzers achieve high power densities and are compact, making them a cost-effective technology for dynamic load operation. Still, PEM electrolysis has not yet been established in terms of large-scale industrial use and is therefore a subject of ongoing research efforts.

While electrolyzers can quickly adapt their production rate [5,6], the load changes induce potentially undesirable stack temperature changes. To hold the stack temperature at a predefined value, simple Proportional–Integral–Derivative (PID) control methods are not effective [4,7] due to the strong non-linearity of the electrolyzer dynamics. Moreover, the increasing thermal mass associated with scaling into the MW class exacerbates the challenge. Various control methods, particularly model predictive control (MPC) for stack temperature control, prove to be viable [8,9]. However, due to heightened computational demands, this form of control is seldomly employed in practical applications. As an alternative to MPC, control methods can be implemented where load variation disturbance is compensated through feed-forward tracking control [4,10,11] using a model of the electrolyzer. In particular, when used in conjunction with the adaptive adjustment of control parameters across different operating ranges, favorable outcomes can be achieved [4,12,13].

However, if the temperature is controlled properly, effective operational management strategies for optimization and consequently cost reduction in electrolyzers are possible. For example, Scheepers et al. [14] optimize the temperature for PEM electrolyzers to improve the conversion efficiency. Such static techno-economic optimizations and analyses are often based on simulations and provide only recommendations for

operational strategies [15–18]. The optimization of PEM electrolyzers via dynamic operation, particularly in conjunction with renewable energy sources such as wind and photovoltaics, has been explored in various studies [19–21]. Although the operation is highly dynamic in response to varying load conditions, many strategies documented in literature aim to maintain the temperature at a predetermined set-point [16,20]. However, slow temperature dynamics increase the flexibility of effective operational management strategies for electrolyzers, which play a crucial role in overall system efficiency. Slow temperature dynamics can be on the order of hours [22] and thus allow for operating in a power range that is not feasible in steady state because the heat production would be too high for the available cooling capacity. Still, if the temperature is reduced during times of high electricity prices, where a low production rate is desired, the electrolyzer can subsequently operate in overload for a scheduling-relevant amount of time (Fig. 1(a)).

Operating in this temperature-overload range is economically beneficial as it allows better use of varying electricity prices. During low (or even negative) electricity prices, operation above the steady-state-feasible power $P^{\max, \text{steady}}$ is feasible as long as the temperature is below the maximum temperature T^{\max} (compare to Fig. 1(a)). The slower the temperature dynamics the longer a power above $P^{\max, \text{steady}}$ is feasible. On the other hand, fast temperature dynamics would mean that once the power is above the steady-state-feasible power $P^{\max, \text{steady}}$ the temperature increases to the maximum T^{\max} and higher powers are not feasible for a relevant amount of time. For high temperature dynamics also additional heating power would be needed, which results in increased operation and investment costs. As stated in Section 2.1.1 our developed method only focuses on cooling power during dynamic load changes. Moreover, high-temperature dynamics can lead to thermal stress and maybe damaging the PEM-Stack.

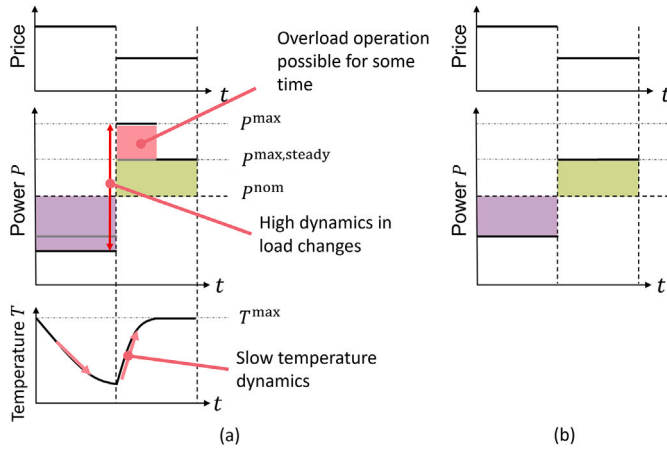


Fig. 1. (a) Using high dynamics in load changes and slow temperature dynamics to increase the electrolyzer's flexibility: During times of high prices, production rates and so power P are reduced substantially below the nominal power P^{nom} , which allows a reduction of the temperature T . Consequently, at times of low prices, an operation above the steady-state-feasible power $P^{\text{max,steady}}$ is possible until the maximum temperature T^{max} is reached. (b) Benchmark case in which temperature dynamics were not taken into account and the power was limited by the steady-state-feasible power.

To achieve the discussed economic advantages, following the required temperature profile is key to ensuring good performance. Thus, for practical operation of electrolyzers accurate temperature tracking performance is required. In terms of overload operation, several commercially available electrolyzers are capable of operating under such conditions for a limited duration [23]. For example, Flamm et al. [24] analyzed a commercially available electrolyzer with 100 kW rated power that could operate at 200 kW for limited amounts of time. During this overload operation, the electrolyzer heated up and had to be cooled later. Similarly, the Energy Park Mainz has electrolyzers with a 4 MW rated power but can operate at 6 MW for up to 15 min [25]. Studying a chlor-alkali electrolyzer, Simkoff and Baldea [26] took this possibility for overload operation into account in a scheduling optimization but used a data-driven surrogate model to approximate the nonlinear temperature dynamics. Alternatively, the integral over the power in overload [27] or the current in overload [24] was used as a proxy for temperature evolution. However, the produced heat is, in principle, a nonlinear function of power/current and is also temperature-dependent [28,29]. Thus a nonlinear optimization would be desirable to capture the actual physics and reduce safety margins. At the same time, electrolyzers have a minimum allowable current below which they should not operate in order to avoid degradation [30]. Consequently, if the possibility of turning the electrolyzer off would need to be considered, a discrete variable would be needed during scheduling optimization.

In our previous research [31,32], we presented dynamic ramping constraints for the demand response scheduling of electrolyzers with slow temperature dynamics. These dynamic ramping constraints exactly reformulated the nonlinear temperature dynamics into linear dynamics with nonlinear constraints using a variable transformation which was possible because the temperature dynamics were differentially flat [33,34]. As nonlinear constraints are approximated on the safe side by piecewise affine functions, we can formulate a mixed-integer linear program (MILP) that can be efficiently optimized and guarantees that the resulting temperature dynamics are feasible with respect to the original nonlinear process model. Thus, we can reduce the temperature during times of low production and allow an overload production, increasing flexibility. Still, the dynamic ramping method was only studied via simulations in our previous research [31,32].

In this paper, we experimentally validate the dynamic ramping approach for electrolyzers with slow temperature dynamics. For this purpose, three different underlying controllers are developed and compared to implement the results of the scheduling optimization. The controllers utilize the temperature profile, from the top layer, as the input and ensure accurate temperature tracking performance while effectively rejecting disturbances from load variations. The main contributions of this publication method lie in the following key areas:

- Enhanced economic viability of PEM electrolyzers under fluctuating electricity market conditions.
- Experimental validation of real-time scheduling optimization for transient operation in PEM electrolyzers.
- Improved cost efficiency and scalability of 2 MW industrial-scale PEM electrolyzers through simulation-based evaluation.

Section 2 provides a detailed description of the experimental test bench and the electrolyzer model. In Section 3, we present our dynamic ramping scheduling optimization method, within three stack temperature control strategies. Section 4 presents the case study, which is subsequently followed by an analysis of the results in Section 5. The implications of aging are discussed in Section 6, while Section 7 delivers the concluding remarks.

2. Electrolyzer system

All practical measurements were conducted at the IET-4 at the Forschungszentrum Jülich. A PEM electrolyzer with an electrical power capacity of 100 kW was employed. The system configuration was as follows: The core of the PEM electrolyzer was the electrochemical PEM cell, consisting of a stack of 27 cells with a cell area of 300 cm². The nominal operating point was set to 3 A/cm² and 2 V. What made the setup unique was the use of the desired input power. To provide the 100 kW, two stacks of 50 kW each were used, which allowed the cell area to be kept small, ensuring optimal sealing of the produced hydrogen up to 50 bar. Fig. 2 shows the 100 kW system with the 50 kW stacks. The specifications of the stacks used are provided in Table 6 in the Appendix.

2.1. Test bench

Fig. 3 depicts the process engineering setup of the 100 kW system.

The PEM electrolyzer consisted of the PEM stack where the electrochemical reaction took place. For this purpose, deionized water was circulated on both the anode and cathode sides through two circulation pumps. On the anode side, water serves as the reactant for splitting water. To control the electrochemical reaction, the current density j_{el}

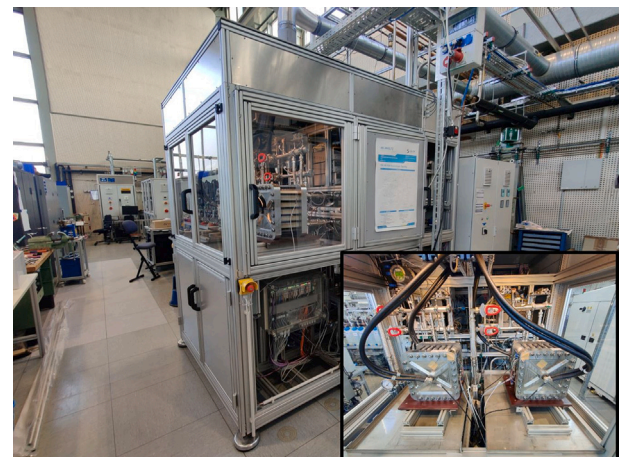


Fig. 2. 100 kW PEM electrolyzer.

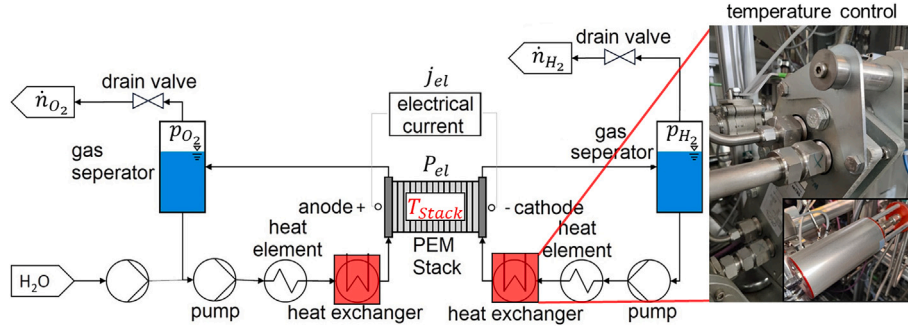


Fig. 3. Flow diagram of the 100 kW PEM electrolyzer.

was used as an input to the stack. This current density j_{el} resulted in a stack voltage U_{Stack} , which forms the input power $P_{el} = j_{el} U_{Stack}$ as a product.

From the electrochemical reaction, we obtained the product gas flow \dot{n}_{H_2} on the cathode and \dot{n}_{O_2} on the anode side. The gas separator tanks separate the water–gas mixture. With the drain valves, the pressure p_{H_2} and p_{O_2} on each side could also be controlled.

In addition to the generated hydrogen, heat was produced, which in turn heats up the PEM stack. To control the temperature, circulation using water as a medium on both sides facilitates the transfer of energy in the form of heat. Each side was equipped with a plate heat exchanger (red boxes in Fig. 3) and a heating element. This setup allows control of the stack temperature T_{Stack} to a predetermined set point depending on the operating point. The summarized operating conditions of the 100 kW PEM electrolyzer are detailed in Table 7 in the Appendix. Section 2.1.1, below, deals with the stack temperature control.

2.1.1. Stack temperature control

Heating elements were used to achieve the operating temperature in the cold start scenario. As this paper primarily focuses on cooling power during dynamic load changes, this aspect is not further elaborated upon here. Cooling power is realized through plate heat exchangers. The 100 kW electrolyzer operates with the cooling power design of a single heat exchanger set at 18 kW. Using two heat exchangers on the anode and cathode sides enables a total cooling power of 36 kW. The volumetric flow on the primary side of the heat exchanger was adjusted to meet the specifications of the heat exchanger and the electrochemical reaction. On the secondary side, the flow of the cooling medium, water, can be regulated to dissipate a specific amount of heat. In order to achieve precise cooling power, represented by $\dot{Q}_{control}$, the cooling medium was maintained at a constant temperature of 6 °C. The linear relationship between the control valve's set point and the heat exchanger's power was achieved through the deployed valve. The control valve used and the heat exchanger are illustrated on the right-hand side of Fig. 3.

The control algorithm commonly used in the 100 kW system to regulate the stack temperature is based on a higher-level control method, the model-based feed-forward control, designed in [4]. The control relies on two subtasks: The first instance calculates the required heat quantity using the PEM electrolyzer model and delivers it to the PEM stack. The second is based on a PID control, adjusting existing differences between the model and reality. Section 3.3 discusses the control algorithm in more detail.

2.2. Model

To investigate the thermal dynamics, the 100 kW system was modeled, encompassing both its electrochemical and thermal behavior. The electrochemical aspects serve as the foundation for each electrolysis cell. The thermal behavior is modeled by the energy flows within the system

and the heat losses to the surroundings. The next two sections delve into this subject.

2.2.1. Electrochemical model

The Nernst voltage U_{nernst} constitutes the foundation of every electrochemical cell. It delineates the minimal voltage required, under ideal conditions, to split water into its constituent elements, hydrogen and oxygen. The following equation:

$$U_{nernst} = \frac{\Delta G^0}{2F} + \frac{R_{gas}T}{2F} \ln \left(\frac{p_{H_2}}{p_{H_2}^{ref}} \sqrt{\frac{p_{O_2}}{p_{O_2}^{ref}}} \right) \quad (1)$$

reveals that the Nernst voltage is influenced by various factors such as Gibbs energy ΔG^0 , partial pressures p_{H_2} and p_{O_2} , and the respective temperature T . The constants R_{gas} and F are given in Table 5. The reference pressures $p_{H_2}^{ref}$ and $p_{O_2}^{ref}$ are defined as the ambient pressure.

However, the PEM electrolysis cell encounters additional resistances that must be overcome to enable electrical current flow in the cell: Firstly, activation losses, induce the need for the overpotential η_{act} , which can be described by the Butler–Volmer equation. Given that in PEM electrolysis, the potential on the cathode side can be neglected, the Butler–Volmer equation can be simplified as follows:

$$\eta_{act} = \alpha \ln \left(\frac{j_{el}}{j_0} \right) \quad (2)$$

This overpotential η_{act} then only depends on the charge transfer coefficient α , the exchange current density j_0 , and the actual electrical current density j_{el} . With in this work we experimental obtained the parameters j_0 and α , shown in Table 5. The flow of electric current introduces additional ohmic losses. To summarize, the ohmic losses in the cell excite two mandatory elements. The primary components of these losses can be characterized by contact resistances R_{con} and membrane resistance R_{mem} . The resulting overvoltage losses are consolidated in:

$$U_{ohm} = (R_{mem} + R_{con})j_{el} \quad (3)$$

All parameters associated with ohmic losses were determined in conjunction with practical experiments and are documented in Table 5.

The final concentration overvoltage is characterized by the under-supply of electrochemical reactants. In the case of large-scale PEM stacks, local distribution effects might occur, which, however, can be mitigated through an appropriate stack design and reactant supply [4,35]. Therefore, concentration overvoltage does not play a role in the modeling process.

If we now combine all overpotentials, the resulting outcome is the cell voltage represented in the following equation:

$$U_{cell} = U_{ohm} + U_{nernst} + \eta_{act} \quad (4)$$

The required power for water-splitting can thus be represented by the current density j_{el} and the resulting cell voltage U_{cell} . Additionally,

a temperature dependency on the cell voltage U_{cell} can be observed through Eq. (2), which constitutes a significant factor attributed to the thermal behavior of the cell and stack. In summary, the cell voltage depends on the current density j_{el} (U_{ohm} , η_{act}), temperature T (U_{nernst}), and the pressures p_{H_2} , p_{O_2} (U_{nernst}). The pressures p_{H_2} , p_{O_2} were maintained constantly during operation. Thus, for control purposes, the cell voltage can be seen as a function of the current density j_{el} and temperature T . Based on the cell voltage $U_{cell}(j_{el}, T)$, the electric input power P_{el} for an entire PEM-Stack can be calculated using the active cell area A_{cell} , the temperature of the stack T_{Stack} , and the number of individual cells N_{cell} :

$$P_{el} = j_{el} \cdot A_{cell} \cdot U_{cell}(j_{el}, T) \cdot N_{cell} = f(j_{el}, T_{Stack}) \quad (5)$$

2.2.2. Adapting the model to aging

For the experiments in the present publication, we start with the model parameters from our previous work [4]. However, we experienced an aging leading to a root mean square error (RMSE) in the cell voltage U_{cell} of 0.028 V and a maximum error of 0.064 V (Fig. 4). To compensate, we introduce two correction factors a_1 , a_2 into the calculation of the cell voltage (compare to Eq. 4):

$$U_{cell} = a_2 U_{ohm} + U_{nernst} + a_1 \eta_{act} \quad (6)$$

With least-squares regression, we determine the correction factors to $a_1 = 0.915$ and $a_2 = 1.31$. The adapted model has a RSME of only 0.0027 V and a maximum error of 0.017 (Fig. 4). Aging effects and the adaptation of the model are further discussed in Section 6.

2.2.3. Thermal model

For the thermal model of the electrolyzer, all energy flows $\sum_k \dot{Q}_k$ into and out of the system boundary are required. To control the resulting temperature changes, the cooling power $\dot{Q}_{control}$ from Section 2.1.1 was used as the control variable. With the total heat capacity C_{100kW} , the temperature changes are given according to the energy balance:

$$\dot{T}_{Stack} = \frac{\sum_k \dot{Q}_k + \dot{Q}_{control}}{C_{100kW}} \quad (7)$$

All parameters for the 100 kW PEM system can be found in Table 5. The generated hydrogen contains the energy that electrochemically exits the system on the cathode side. Here, the electrical current density j_{el} is of crucial importance. Moreover, the number of cells N_{cell} and the active cell area A_{cell} play a decisive role, and the generated hydrogen flow can be determined through Faraday's law, shown in the following equation:

$$\dot{n}_{H_2} = N_{cell} \cdot A_{cell} \cdot \frac{j_{el}}{2F} \quad (8)$$

The oxygen produced on the anode side is given as:

$$\dot{n}_{O_2} = N_{cell} \cdot A_{cell} \cdot \frac{j_{el}}{4F} \quad (9)$$

If the energetic content of the hydrogen is utilized, the resulting energy flow can be derived from Eq. (8) to yield:

$$\dot{Q}_{H_2} = N_{cell} \cdot A_{cell} \cdot \frac{j_{el}}{2F} \cdot \Delta H_{HHV, H_2} \quad (10)$$

In this study, the higher heating value of the hydrogen $\Delta H_{HHV, H_2}$ was utilized. However, not only hydrogen leaves the system on the cathode side. Due to the operating temperature T_{Stack} of PEM electrolysis, the existing hydrogen becomes saturated with water vapor. The saturation vapor pressure $p_{H_2, satt}$ on the cathode side, as well as on the anode side $p_{O_2, satt}$, were determined as per [36]. With the given parameter in Table 5, the pressure on the cathode p_K and anode sides p_A and the heat of vaporization water, the amount of energy leaving the system as water vapor can be formulated with:

$$\dot{Q}_{Steam} = - \left(\frac{p_{H_2, satt}}{p_K - p_{H_2, satt}} \cdot \dot{n}_{H_2} + \frac{p_{O_2, satt}}{p_A - p_{O_2, satt}} \cdot \dot{n}_{O_2} \right) \cdot (d_1 \cdot T_{Stack} + d_2) \quad (11)$$

The consumed water for water electrolysis must be reintroduced into the system. The supplied water has the surrounding temperature and must be heated to the electrolyzer's operating temperature. Additionally, a certain portion of the water permeates from the anode to the cathode side. In the case of the 100 kW PEM system, the permeated water is discarded and thus must also be supplied to the system. The drag factor D represents the water permeation and is stated in Table 5. The resulting mass flow of the total water can be determined as follows:

$$\dot{m}_{H_2O} = M_{H_2O} \cdot \dot{n}_{H_2} \cdot (1 + 2D) \quad (12)$$

To heat up the supplied water, the energy flow is calculated with:

$$\dot{Q}_{H_2O} = \dot{m}_{H_2O} (T_{Stack} - T_{surr}) \cdot c_{H_2O} \quad (13)$$

Finally, the only remaining aspect is the energy flow, which is dissipated into the surroundings. A crucial factor in this process is the thermal capacitance and thermal resistance to the surroundings. These two significant elements play a substantial role in the subsequent temperature dynamics within the electrolyzer. The heat dissipation to the surroundings is

$$\dot{Q}_{sur} = (T_{Stack} - T_{surr}) \cdot R_{HT100kW} \quad (14)$$

With $R_{HT100kW}$, the thermal resistance to the surroundings is given. This parameter is specific for each electrolyzer and is presented in Table 5 for the 100 kW electrolyzer.

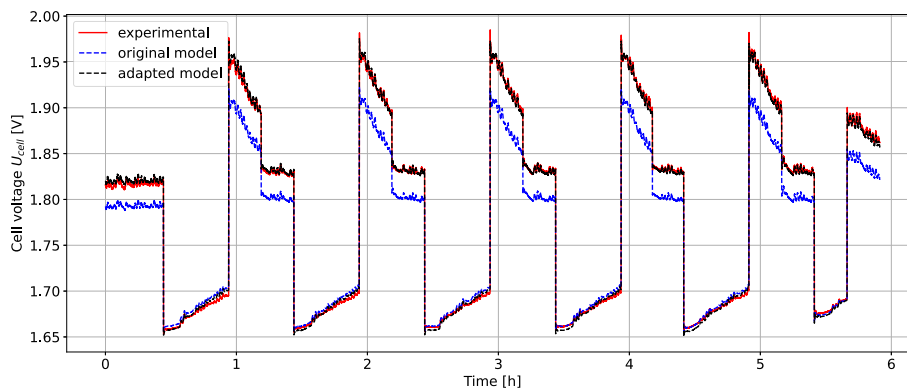


Fig. 4. Comparison of original and adapted model to experimental data.

To summarize, the entire energy flow into and out of the balancing space is given as:

$$\sum_k \dot{Q}_k = P_{el} + \dot{Q}_{H_2} + \dot{Q}_{Steam} + \dot{Q}_{H_2O} + \dot{Q}_{sur} \quad (15)$$

For control purposes, this means that the derivative of the temperature \dot{T}_{Stack} is a function of the temperature T , the current density j_{el} , and the control variable $\dot{Q}_{control}$ (compare to Eq. 7).

2.3. Limiting cooling power

As our electrolyzer is a test bench with a relatively low rated power, the cooling power was designed to be on the conservative side, i.e., it is always sufficient to maintain the electrolyzer below a maximum stack temperature of $T_{Stack}^{max} = 80^\circ\text{C}$. We define the maximum electrical input power as the power at $T_{Stack}^{max} = 80^\circ\text{C}$ and the maximum current density of $j_{el}^{max} = 2\text{ A/cm}^2$. This power is $P_{el}^{max} = 62.9\text{ kW}$.

As the overload operation of commercially available electrolyzers is caused by limited cooling capacities, we limited the cooling power of our test bench to mirror the same conditions. For available electrolyzers, the nominal, i.e., steady-state-feasible, power was reported to be 50 % [24] or 2/3 [25] of the maximum power. Here, we define a nominal power of $P_{el}^{nom} = 50.3\text{ kW}$, which is 80 % of the maximum power P_{el}^{max} . Thus, we are on the conservative side with respect to the overload potential.

As the maximum cooling power is $\dot{Q}_{control}^{max}$, we define the cooling needed to keep the electrolyzer temperature in steady-state at the nominal power P_{el}^{nom} and the maximum temperature T_{el}^{max} . This cooling power is $\dot{Q}_{control}^{max} = 3.6\text{ kW}$. In the following, we limit the available cooling power to $\dot{Q}_{control}^{max}$ even if our test bench would, in principle, permit higher cooling to simulate the conditions in commercially available electrolyzers for which overload operation is interesting.

Based on this setup, we can demonstrate how scheduling optimization with dynamic ramping constraints can optimize the electrolyzer's temperature and make use of overload operation.

3. Method

Our method includes both the economic scheduling optimization and control of the electrolyzer. In the following, we first present this approach (Section 3.1) and then discuss the scheduling optimization (Section 3.2) and control separately (Section 3.3).

3.1. Integrated scheduling and control approach

The traditional scheduling and control structure where scheduling considers steady-state models is not applicable here, as the slow temperature dynamics are scheduling-relevant, i.e., on the same timescale as electricity prices. Thus, an approach is needed to integrate scheduling and control [37,38]. These approaches can be classified into bottom-up and top-down approaches [39]. An example of a bottom-up approach that leads to full integration is economic model predictive control (MPC) [40]. For our problem, such an economical MPC would have to optimize the slow nonlinear temperature dynamics and, at the same time, reject fast disturbances (Fig. 5, left). However, due to the fact that the PEM electrolyzer has strongly nonlinear temperature dynamics, optimization problems for this kind of system are hard to solve, whereas fast disturbances require frequent re-calculation. Note that discrete on/off-decisions also introduce integer variables such that the optimization problem is a nonlinear mixed-integer linear problem (MINLP). Such dynamic MINLPs can typically not be solved within seconds, which would, however, be needed for a disturbance rejection. Thus, we do not focus on the economical MPC approach in the following.

In order to avoid this MINLP, we chose a top-down integration approach that includes dynamics in scheduling but still splits the problem into two sub-tasks [39] (Fig. 5, right). The upper layer focuses on the scheduling optimization with dynamic ramping constraints. This approach has the chief advantage, that we can perform the economic

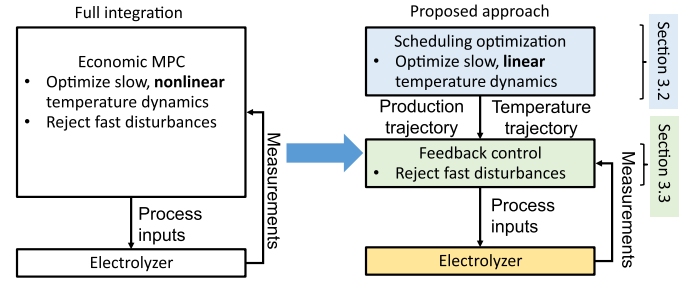


Fig. 5. Comparison of full integration of scheduling and control with an economical model predictive control (MPC) and the proposed top-down approach, which maintains task separation between scheduling and control.

optimization in the coordinate space of the process outputs where temperature dynamics are linear, which is discussed in Section 3.2 and leads to an easier-to-solve mixed-integer linear problem (MILP). Utilizing the available results from the dynamic scheduling optimization the bottom layer implements an appropriate control methodology to ensure accurate temperature tracking performance while effectively compensating disturbances from load variations. Due to this underlying controller, the economic optimization from the upper layer can be performed less frequently, which leads to an additional advantage of the approach. In Section 3.3 three control methods are introduced for identifying a suitable control method to guarantee the desired temperature tracking performance of the optimization.

3.2. Scheduling using dynamic ramping

In this section, we summarize the dynamic ramping approach, which allowed us to reformulate the nonlinear temperature dynamics of the electrolyzer into a mixed-integer linear formulation. As this reformulation was based on our previous work [31,32], where the reformulation was studied based on simulations, we only summarize it briefly here.

The principle of dynamic ramping constraints is to reformulate a nonlinear dynamic process model with linear constraints into a linear dynamic model with nonlinear ones. Subsequently, these nonlinear constraints are approximated conservatively by means of piecewise affine (PWA) constraints. The conservatism of the PWA constraints ensures that the resulting operation is feasible with respect to the original nonlinear process model. At the same time, the PWA constraints can, in principle, approximate the true nonlinear aspect to any degree of accuracy. Note that the reformulation into dynamic ramping constraints is, in general, possible for a dynamic model, which is differentially flat as flatness implies that there is a coordinate transformation to a coordinate space in which the dynamics are linear [33,34].

As a result of the dynamic ramping reformulation, the decision variables in the optimization are the hydrogen production rate \dot{n}_{H_2} and the temperature derivative of the stack temperature \dot{T}_{Stack} . The dynamic ramping constraints limit the stack temperature \dot{T}_{Stack} by upper and lower limits that are PWA functions of the hydrogen production rate \dot{n}_{H_2} and the stack temperature T_{Stack} :

$$\dot{T}_{Stack, PWA}^{min}(\dot{n}_{H_2}, T_{Stack}) \leq \dot{T}_{Stack} \leq \dot{T}_{Stack, PWA}^{max}(\dot{n}_{H_2}, T_{Stack}) \quad (16)$$

Further details on the dynamic ramping reformulation are given in the Appendix and our previous publications [31,32].

For the electric input power, which is needed to calculate the cost of operation, we use a linear approximation:

$$P_{el, lin}(\dot{n}_{H_2}, T_{Stack}) = a_0 + a_{\dot{n}_{H_2}} \dot{n}_{H_2} + a_T T_{Stack}, \quad (17)$$

with parameters $a_0, a_{\dot{n}_{H_2}}, a_T$ that are fitted to the original model. Note that if a linear approximation would not be accurate enough a PWA

approximation can be used for the electric input power of electrolyzers [24].

The derived dynamic ramping constraints can be incorporated into a mixed-integer linear optimization with an economic objective function. The explicit representation of temperature dynamics allows us to represent the flexibility to operate in overload for a certain period of time. In the following, we discuss the economic optimization performed in this study to test the concept.

3.2.1. Economic scheduling optimization

In a typical demand response case [6,41], the electrolyzer must produce a nominal production rate $\dot{n}_{H_2}^{nom}$ on average over the time horizon $[t_0, t_f]$ but can flexibly schedule its production volume as a reaction to the financial incentives given by electricity markets. The optimization problem for scheduling the electrolyzer's operation is summarized in the following:

$$\min_{\dot{T}_{Stack}(t), \dot{n}_{H_2}(t)} \int_{t_0}^{t_f} pr(t) P_{el,lin}(\dot{n}_{H_2}(t), T_{Stack}(t)) dt \quad (Pa)$$

$$\text{s.t. } \dot{T}_{Stack, PWA}^{min}(\dot{n}_{H_2}(t), T_{Stack}(t)) \leq \dot{T}_{Stack}(t) \leq \dot{T}_{Stack, PWA}^{max}(\dot{n}_{H_2}(t), T_{Stack}(t)) \quad (Pb)$$

$$\forall t \in [t_0, t_f] \quad (Pb)$$

$$z_{on}(t) \dot{n}_{H_2}^{min} \leq \dot{n}_{H_2}(t) \leq z_{on}(t) \dot{n}_{H_2}^{max} \quad \forall t \in [t_0, t_f] \quad (Pc)$$

$$\int_{t_0}^{t_f} \dot{n}_{H_2}(t) dt = \dot{n}_{H_2}^{nom} (t_f - t_0) \quad (Pd)$$

$$T_{Stack}(t_0) = T_{Stack,0} \quad (Pe)$$

$$T_{Stack}^{min} \leq T_{Stack}(t) \leq T_{Stack}^{max} \quad \forall t \in [t_0, t_f] \quad (Pf)$$

The objective is to minimize the electricity costs, which are the integral over the electricity price $pr(t)$ and electric power $P_{el,lin}(\dot{n}_{H_2}(t), T_{Stack}(t))$ (compare to Eq. 17) (Pa). The time derivative of the temperature $\dot{T}_{Stack}(t)$ is limited by the PWA dynamic ramping constraint (compare to Eq. 24 and Fig. 19) (Pb). The binary variable $z_{on}(t)$ ensures that the electrolyzer either produces hydrogen between the minimum and maximum production rates $\dot{n}_{H_2}^{min}$, $\dot{n}_{H_2}^{max}$ or is off (Pc). Eq. (Pd) ensures that the nominal production $\dot{n}_{H_2}^{nom}$ is reached on average over the time horizon $[t_0, t_f]$. Finally, Eq. (Pe) states the initial temperature $T_{Stack,0}$, and Eq. (Pf) ensures that it stays within its limits T_{Stack}^{min} , T_{Stack}^{max} .

Using discretization with collocation on finite elements [42,43], the optimization Problem (P) is converted into an MILP, which we solve using Gurobi [44]. The result of this scheduling optimization problem is a trajectory for the temperature $T_{Stack}(t)$, the time derivative of the temperature $\dot{T}_{Stack}(t)$, and the hydrogen production \dot{n}_{H_2} . These quantities are passed as set-points to the underlying control discussed in the following section.

3.3. Control methods

In Section 2.1.1, the control method utilized for stack temperature control in the 100 kW PEM electrolyzer was briefly described. The control strategy employed, involving adaptive PID control, is further elaborated upon in this section, as it was applied during operation of the PEM electrolyzer.

As the main novelty of this publication, Section 2.2.3 addresses the dynamic ramping and associated time derivative of the stack temperature \dot{T}_{Stack} . This temporal variation in stack temperature is also intended to be integrated into the existing control algorithm and utilized as a feed-forward control strategy. We compare two model-based feed-forward control strategies: one with a static model and one with a dynamic model.

Finally, these two feed-forward controls are compared with a purely adaptive PID control. This section introduces all three control methods that we compared in this study.

3.3.1. Static model-based feedforward adaptive PID control

First, we introduce the static version of the feed-forward control, which was used in our previous publication [4]. The principle of the higher-level control strategy with static model-based feed-forward and adaptive PID control is shown in Fig. 6. This general control method was used during normal operation of the 100 kW PEM electrolyzer and was developed in [4]. For our special case of dynamic ramping, the initial set-points for the control algorithm are derived from the economic scheduling optimization outlined in Section 3.2.1. The result of this optimization problem is a trajectory of set-points for the time-derivative temperature \dot{T}_{Stack}^{SP} and the hydrogen production $\dot{n}_{H_2}^{SP}$. With the integration of \dot{T}_{Stack}^{SP} , the set-points of the temperature T_{Stack}^{SP} are also given. The proportional relationship between $\dot{n}_{H_2}^{SP}$ and j_{el}^{SP} can be determined with Eq. (8) in Section 2.2.3.

The control algorithm itself relies on two sub-tasks: With Eq. (7) from Section 2.2.3, it can be directly seen that if $\dot{Q}_{control}$ is equal to $\sum_k \dot{Q}_k$ the stack temperature must be constant. Thus, the time derivative of the temperature as a given set-point can be neglected for our static calculation. If no changes in temperature take place, Eq. (23) can be reformulated as follows:

$$\dot{Q}_{Control}^{nom} = f(T_{Stack}^{SP}, j_{el}^{SP}) \quad (18)$$

With this equation, the nominal cooling power $\dot{Q}_{control}^{nom}$ for temperature equilibrium can be determined for the given set-points T_{Stack}^{SP} and j_{el}^{SP} of the scheduling optimization. The control algorithm uses this model-based calculation in the first instance and delivers $\dot{Q}_{control}^{nom}$ in the second. Thus, the nominal cooling power is only given for a static operating condition with no changes in temperature or feedback from process variables.

The second control sub-task is to compensate for differences between the model and reality. For this sub-task, a PID-controller is used. To identify the best PID parameters, the model of the PEM electrolyzer was linearized under different operating conditions. For each operating condition, the optimal parameters were identified and are presented in Table 8 in the Appendix. Consequently, the PID parameters of the control algorithm were adapted depending on operating conditions given by the current density set-point j_{el}^{SP} and the actual stack temperature T_{Stack} . The output of the PID algorithm $\Delta \dot{Q}_{control}$ closes the gap between the nominal defined cooling power via the model and the real cooling power needed to keep the temperature at its set-point. The summary of

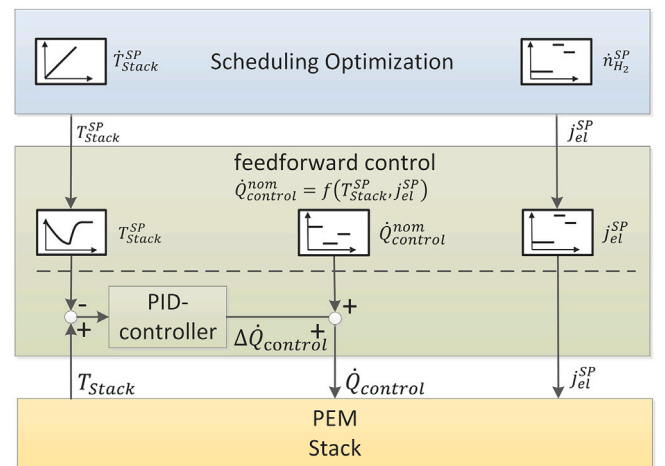


Fig. 6. Static model-based feed-forward with adaptive PID control for a 100 kW PEM electrolyzer. Based on the set-points for temperature T_{Stack} and hydrogen production rate $\dot{n}_{H_2}^{SP}$, the control sets the cooling power $\dot{Q}_{control}$ and current density j_{el} .

both instances forms the manipulated variable $\dot{Q}_{control}$, which enters the PEM system.

The model-based feed-forward algorithm of this control strategy only deals with constant stack temperatures. For dynamic ramping, it is also intuitive to take temperature changes into consideration for calculations. The next section provides more details regarding this type of control algorithm primarily, exploring dynamic approaches through temperature changes.

3.3.2. Dynamic model-based feedforward adaptive PID control

To exploit the full power of the dynamic ramping approach, the feed-forward algorithm from Section 3.3.1 is expanded to include dynamic changes in stack temperature. Thus, the derivative \dot{T}_{Stack}^{SP} for the given set-points of the temperature T_{Stack}^{SP} is now taken into consideration. If we follow the same procedure from Section 3.3.1 and take time-dependent temperature changes into account, Eq. (23) can be written as follows:

$$\dot{Q}_{Control}^{nom} = f(\dot{T}_{Stack}^{SP}, T_{Stack}^{SP}, j_{el}^{SP}) \quad (19)$$

The determined nominal cooling power $\dot{Q}_{Control}^{nom}$ now also depends on temperature changes arising from the scheduling optimization. This additional dependency is used not only to determine the nominal cooling power for static operating points during operation but also the nominal cooling power required over time to optimally follow temperature changes. This dynamic feed-forward approach can be advantageous under strong dynamic conditions and can significantly improve stack temperature control. Fig. 7 shows the additional dependency of \dot{T}_{Stack}^{SP} within the control algorithm. The rest of the control algorithm remains the same as that under the static conditions outlined in Section 3.3.1.

3.3.3. Adaptive PID control

Finally, in order to check the effect of the feed-forward control, we study a case in which only the adaptive PID algorithm acts to control the stack temperature T_{Stack} (Fig. 8). As conveyed in Sections 3.3.2 and 3.3.1, only the schedule of the PID parameters for different operating conditions remain active (Table 8 in the Appendix). Here, the manipulated variable of cooling power $\dot{Q}_{control}$ only depends on the PID algorithm.

4. Case study

In this section, we summarize the parameters used for the experimental validation of our method. We assume a generic electricity price

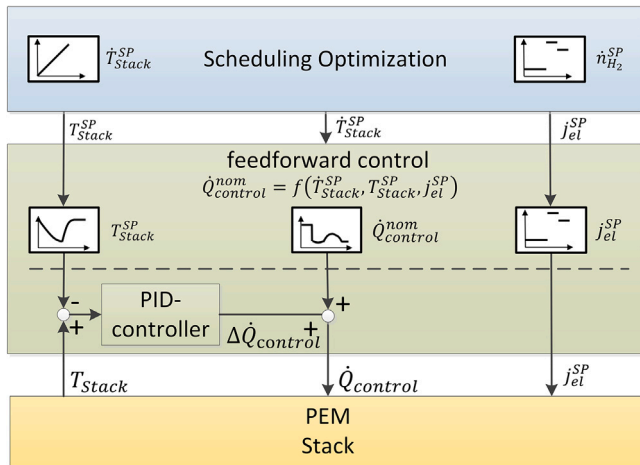


Fig. 7. Dynamic model-based feed-forward with adaptive PID control for 100 kW PEM electrolyzer. Based on the set-points for temperature T_{Stack}^{SP} and hydrogen production rate $\dot{n}_{H_2}^{SP}$, the control sets the cooling power $\dot{Q}_{control}$ and current density j_{el} .

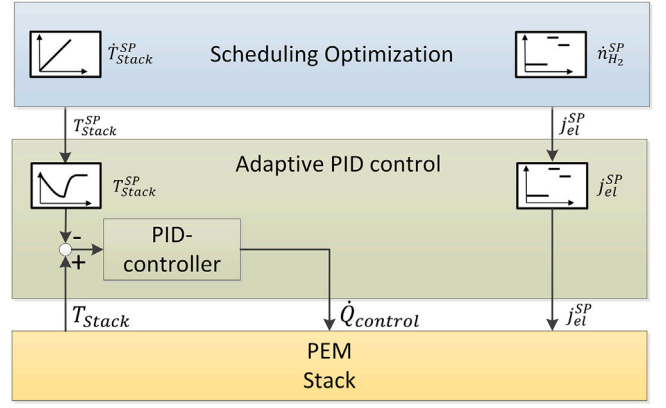


Fig. 8. Adaptive PID control of the 100 kW PEM electrolyzer. Based on the set-points for temperature T_{Stack}^{SP} and hydrogen production rate $\dot{n}_{H_2}^{SP}$, the control sets the cooling power $\dot{Q}_{control}$ and current density j_{el} .

profile with 15-min time steps, as preliminary simulations showed that the temperature dynamics of this 100 kW test bench electrolyzer fall within this time scale. Note that the temperature dynamics of electrolyzers become slower with size, as the thermal capacity increases more strongly than the convective heat losses to the ambient [45]. In Section 5.5, we undertake a simulation-based upscaling in which we compare the performance of our 100 kW test bench to a 2 MW electrolyzer. In this simulation-based assessment, we also vary the price spread between the maximum and minimum electricity prices of our generic price profile.

Following [46], we assume an average utilization rate of 80 % for the electrolyzer. Consequently, the nominal production rate $\dot{n}_{H_2}^{nom}$ (compared to (Pd)) requires a power P^{nom} that is equal to 80 % of the steady-state-feasible power $P^{max,steady}$ (cf. Fig. 1).

We consider the scheduling optimization (P) based on dynamic ramping constraints in two variants: In one, we assume that the electrolyzer can be turned off such that the binary $z_{on}(t)$ in (Pc) is a degree of freedom, whereas in the other, we assume that the electrolyzer must remain active during operation such that the binary $z_{on}(t)$ is fixed to one. We distinguish these two cases because, while turning off the electrolyzer can be economically beneficial, it is technically challenging, as the electrolyzer is operated under pressure. Due to the permeation of hydrogen to the anode side, hydrogen is continuously measured in oxygen to obey the lower explosion limit. This measurement is realized through a bypass with a constant volume flow. If the electrolyzer is turned off, the pressure decreases and the measurement ends. For safety reasons, the system would shut down in such a state.

For both cases, with and without turn-off, we introduced a benchmark case without dynamic ramping constraints. In this benchmark case, the electrolyzer also performed a demand response, but the temperature profile was not optimized. Thus, the electrolyzer was forced to powers below the maximum steady-state-feasible power $P^{max,steady}$. All four cases (dynamic ramping and benchmark with and without turning off) were studied in the simulations. Experimentally, we analyzed the dynamic ramping case with turn-off together with the dynamic feed-forward control (Section 3.3.2) twice. For the dynamic ramping case without turn-off, we experimentally studied all three control methods introduced in Section 3.3, as the simulations show that the effect of the feed-forward control could be especially interesting here. Finally, we considered the benchmark case without turning the electrolyzer off experimentally. Here, we first studied the benchmark with dynamic feed-forward control (Section 3.3.2) and then without a feed-forward control and placed the set-point for the PID control at 80 °C. The experimentally investigated cases are summarized in Table 1.

Table 1
Overview of the conducted experiments.

Experiment	Approach	Turn off	Control
$DR_{DFF}^{with\ off} 1$	Dynamic ramping	Yes	Dynamic feed-forward
$DR_{DFF}^{with\ off} 2$	Dynamic ramping	Yes	Dynamic feed-forward
$B_{DFF}^{no\ off}$	Benchmark	No	Dynamic feed-forward
$B_{PID}^{no\ off}$	Benchmark	No	Pure PID
$DR_{DFF}^{no\ off}$	Dynamic ramping	No	Dynamic feed-forward
$DR_{PID}^{no\ off}$	Dynamic ramping	No	Pure PID
$DR_{SFF}^{no\ off}$	Dynamic ramping	No	Static feed-forward

4.1. Solution times

The scheduling optimization problems are solved using Gurobi version 9.5.2 on an Intel Core i7 processor. The solution time is 10 s without the discrete decision to turn the electrolyzer off and 15 s with this discrete decision. Note that such fast solution times would allow a frequent re-optimization, which could be required in real-time markets.

5. Results

5.1. Experimental validation for the base case

We first discuss the base case with our dynamic ramping method, the possibility of turning the electrolyzer off, and the dynamic feed-forward control (Experiment $DR_{DFF}^{with\ off} 1$ in Table 1). The optimization schedules the power in overload operation at times of the lowest electricity prices, e.g., 1–1.25 h, (Fig. 9). To enable the overload operation, the electrolyzer operates at lower powers half an hour prior, to reduce its temperature. Thus, according to the nonlinear process model, an overload operation is possible for 15 min without violating the maximum temperature of 80 °C (compare with the black curves from simulations displayed in Fig. 9). While the temperature is lowered, the electrolyzer is turned off four times (0.75–1 h, 1.75–2 h, 3.75–4 h, and 4.75–5 h in Fig. 9).

Note that the reduction in temperature during times of low power is partly unavoidable due to lower heat production and partly a decision by the scheduling optimization as can be seen clearly by comparing the dynamic ramping result to the benchmark at hour 2 (Fig. 9), where the electrolyzer operates at the same power for both dynamic ramping and benchmark cases: In the benchmark case, the lower heat production leads to a temperature reduction down to 69 °C. During this temperature reduction, the cooling power is zero as in general higher temperatures are desirable due to higher efficiencies. In contrast, our dynamic ramping approach uses a higher cooling power and cools the electrolyzer down to 58 °C because this lower temperature allows a higher overload operation in the following timestep.

Comparing the simulative and experimental results shows that electrical power is predicted well by the process model (Fig. 9). The stack temperature T_{Stack} can be tracked overall with small deviations in the underlying feed-forward controller. In steady-state operation, the experimental temperature oscillates around the set-point (see, e.g., 0–0.5 h in Fig. 9). This behavior can be explained by unmodeled features of the test bench: Through the electrochemical reaction, as described by Section 2.2.1, water is consumed on the anode side. Additionally, water permeates from the anode side through the membrane to the cathode side (compare to Eq. 12). It is evident that both processes depend heavily on the input power and result in a reduction of water content on the anode side. In the case of our 100 kW electrolyzer, the replenished water is at an ambient temperature and dosed on the anode side through a two-point control algorithm. This process extracts thermal energy from the system, which manifests as periodic fluctuations in stack temperature. The temperature also deviates from the set-point during dynamic operation, which leads to short periods in which the electrolyzer overshoots the maximum temperature of 80 °C. The maximum overshoot is 1.8 °C.

We discuss this main case in detail, as the results for the other experiments were similar. The maximum temperature overshoot is always below 2 °C. Therefore, the overload operation with dynamic ramping constraints is shown to be experimentally feasible for our test bench. If

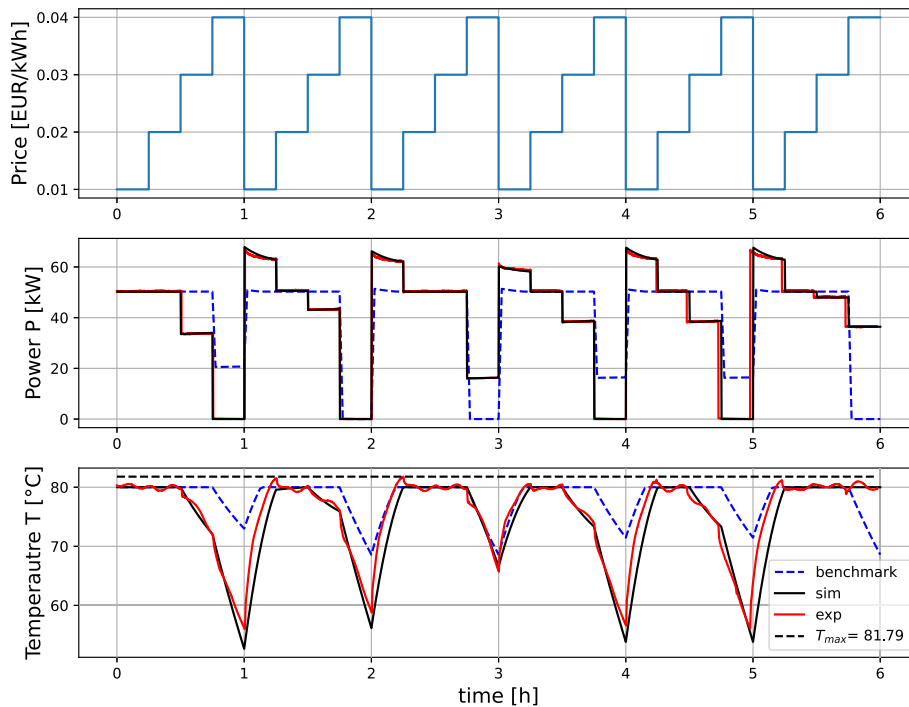


Fig. 9. Electricity price, electric power P , and temperature T for the dynamic ramping case with turn off and dynamic feed-forward control (Experiment $DR_{DFF}^{with\ off} 1$, Table 1). The black curves show the simulation (sim) and the red curves the experiment (exp). Moreover, the simulated benchmark case is shown with blue dashed lines.

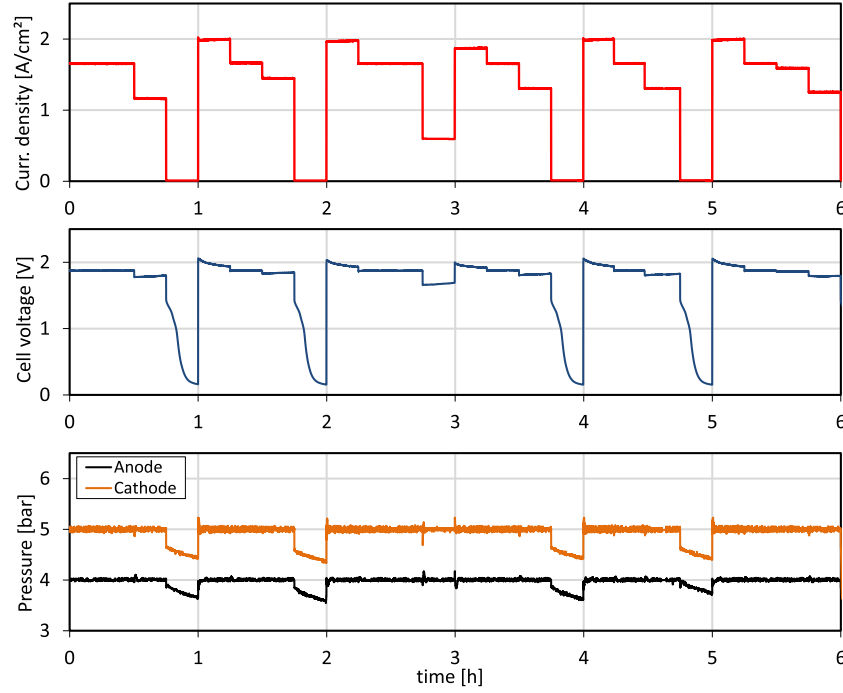


Fig. 10. Trajectory of the process parameters j_{el} , U_{cell} , p_{O_2} and p_{H_2} during operation in dynamic ramping case with turn off and dynamic feed-forward control (Experiment $DR_{DFF}^{with\ off}$ 1, Table 1).

a short overshoot above the maximum temperature of 80 °C is critical, it might be necessary to add a back-off constraint for safety.

Furthermore, Fig. 10 illustrates the progression of additional process parameters during the dynamic ramping case with turn off and dynamic feed-forward control (Experiment $DR_{DFF}^{with\ off}$ 1, Table 1). The values displayed for U_{cell} and j_{el} in the upper part, represent the average measurements across both stacks. When load is turned off, the cell voltage follows a characteristic trajectory; if the load remains on, U_{cell} stays above the electrochemical decomposition voltage of water. The lower section of Fig. 10 shows the pressure on the anode and cathode side. The set-points are defined to $p_{O_2} = 4$ bar and $p_{H_2} = 5$ bar.

5.2. Cost comparison

Whereas the previous section shows that an overload operation with dynamic temperature ramping is feasible, we analyze the economic advantage in this section. Based on the simulations, we predict a substantial cost reduction between the benchmark and dynamic ramping methods. We always express the costs relative to a constant operation at a nominal production rate $\dot{n}_{H_2}^{nom}$. Note that in all variants the amount of hydrogen produced over the time horizon equals $\dot{n}_{H_2}^{nom}(t_f - t_0)$ (compare to Eq. Pd). In the benchmark case, i.e., without making use of temperature dynamics, costs are reduced 12.3 % compared to constant operation (Fig. 11). If the electrolyzer is allowed to be turned off, cost reductions increase to 13.0 %. Using dynamic ramping, as discussed in the previous section, increases the cost reductions to 16.3 % (without turning off) and 16.8 % (with turning off). That is, the simulations show a reduction in cost by dynamic ramping constraints of 3 % and 3.8 %.

We use the experiments to compare the production costs predicted by simulations with the measured cost reductions. The seven experiments agree well with the simulated costs (compare red crosses in Fig. 11 to gray bars). On average, the experimental cost reduction is 0.6 % lower than the simulation, which is a slight difference compared to the difference between the dynamic ramping method and benchmark (3 % and 3.8 % as discussed above).

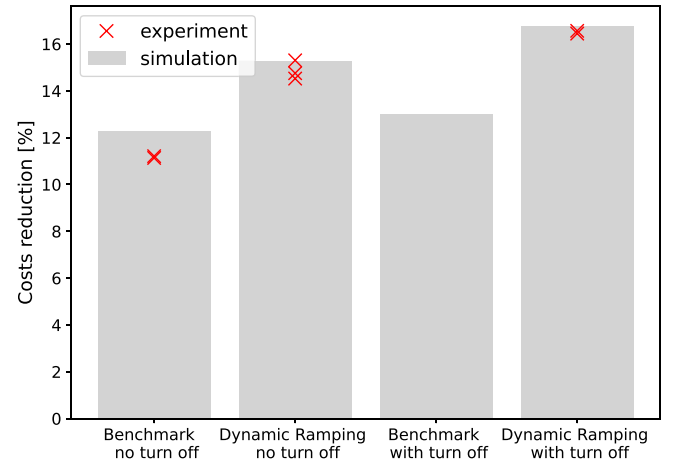


Fig. 11. Cost reduction compared to steady-state operation for different cases. The seven experiments from Table 1 are indicated with red crosses.

These findings provide compelling experimental validation of the economic benefits of dynamic ramping constraints, confirming their potential for improving the cost efficiency of PEM electrolyzer operation under fluctuating electricity market conditions.

5.3. Performance of different controllers

In this section, we compare the different control schemes introduced in Section 3.3. We perform this comparison for the scheduling that does not turn the electrolyzer off because the resulting schedule requires a jump in the simulated cooling power at the beginning of the third quarter of every hour (see Fig. 12 and Figs. 20–22 in the Appendix). This jump in cooling power is caused by the reduction of electric power from 50 to 36 kW while the temperature set-point remains constant. Therefore, the cooling power can be reduced.

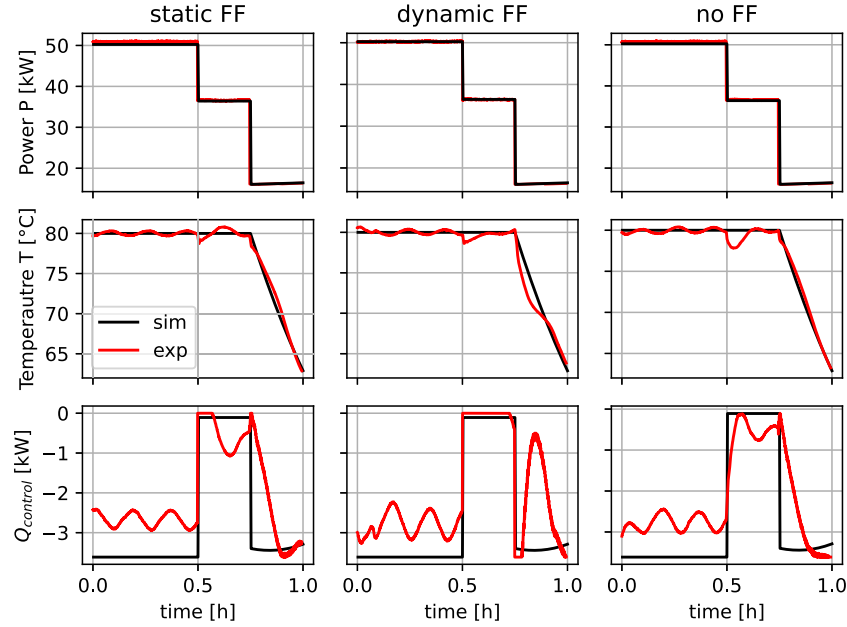


Fig. 12. Comparison of static feed-forward (FF) control, dynamic FF control, and no FF control, showing power, temperature, and cooling power $\dot{Q}_{control}$ for simulation (sim) and experiment (exp.). The case consists of dynamic ramping without turn-off (experiments $DR_{DFF}^{no\ off}$, $DR_{PID}^{no\ off}$ and $DR_{SFF}^{no\ off}$ in Table 1). The full profiles for the experiments are shown in the Appendix.

In the two feed-forward control schemes, this jump in the cooling power is anticipated (Fig. 12, left and middle). With the pure PID control, however, the cooling power only reacts after the temperature deviates substantially from the set-point (Fig. 12, right). Thus, a feed-forward control exhibits advantages in tracking behavior for the stack temperature control when the electric power jumps. Improved tracking is also reflected in the Root Mean Square Error (RMSE). For a quantitative comparison, Table 2 presents the RMSE values of the different control methods over the whole operation time of 6 h (Fig. 9) and for 10 min after power drops from 50 to 36 kW (Fig. 12). In the first 10 min after power drops, the RMSE is 1.18 K with the pure PID control, while it is only 0.61 K with dynamic feed-forward and 0.58 K with static feed-forward control. Thus, anticipating the jump in cooling power allows a closer temperature tracking. Over the complete 6 h-time-horizon, the RMSE is 0.23 K higher for the Pure PID control (2.01 K instead of 1.78 or 1.77, compare to Table 2). Thus, as the addition of feed-forward control results in improved tracking behavior. The dynamic ramping scheduling optimization method is only as good as the performance of the underlying control method allows. Thus, the whole algorithm is highly dependent on the quality of the control method and a feed-forward control can be recommended based on our results. Especially, as applying the dynamic ramping method requires a dynamic temperature model anyhow, and with this model, implementing a feed-forward control is straightforward. In a case with very high dynamic load variations, such as wind and photovoltaics, the effect of the feed-forward control might be even stronger. Between the two feed-forward controls studied, we do not see substantial differences (Table 2).

Table 2
RMSE control methods.

Case			RMSE [K]	
Approach	Turn off	Control	6 h	10 min
Dynamic ramping	No	Static feed-forward	1.77	0.58
Dynamic ramping	No	Dynamic feed-forward	1.78	0.61
Dynamic ramping	No	Pure PID	2.01	1.18

Overall, feed-forward control significantly improves temperature tracking performance in dynamic ramping scheduling, particularly during power transitions, making it the preferred control strategy for PEM electrolyzers operating under fluctuating load conditions.

5.4. Evaluation of the temperature model

The performance of our dynamic ramping constraints depends on the accuracy of the underlying temperature model. As discussed above, the temperature set-point can be tracked effectively. This section compares the cooling power $\dot{Q}_{control}$ between simulation and experiment. Looking at a specific point in time model and experiment differ (cf. Figs. 20–22). These differences can be explained by disturbances acting on the plant, such as freshwater injection, which is explained in detail in Section 5.1.

To compare the overall cooling, we compare the integral over the cooling power $\dot{Q}_{control}$ between simulation and experiment. The overall cooling energy was between 0.5 % and 8.1 % smaller in the experiments compared to the simulations (Table 3). Thus, our model slightly overestimates the cooling energy needed. This overestimation could be explained by the fact that we assume a constant ambient temperature of 25 °C, whereas the temperature in the experimental hall varies and is below 25 °C most of the time. The fact that our model overestimates the required cooling energy might be one reason why the dynamic ramping approach works well experimentally: The overestimation of the required cooling power gives the underlying controller some leeway to reject disturbances. If dynamic ramping is applied with a temperature model that underestimates the required cooling energy, additional backup constraints might be needed to ensure that the controller can track the temperature set-point.

5.5. Simulative study on upscaling

As discussed above, our 100 kW test bench shows relatively fast temperature dynamics. In this section, we compare the advantages of the dynamic ramping method over the benchmark between the 100 kW test bench and a 2 MW electrolyzer in a simulation study. To do so, we use values for the thermal mass and heat transfer coefficient from Ref. [45]. The thermal mass increases from $C_{100kW} = 3.00 \cdot 10^5$ J/K to $C_{2MW} =$

Table 3

Comparison of the integrated cooling power $\int_t \dot{Q}_{control} dt$ between simulation and experiments for the seven conducted experiments (compare to Table 1).

Case	Approach	Turn off	Control	$\int_t \dot{Q}_{control} dt$ [kW h]		Deviation [%]
				Simulation	Experiment	
Dynamic ramping	Yes		Dynamic feed-forward	18.48	17.71	4.1
Dynamic ramping	Yes		Dynamic feed-forward	18.48	17.23	6.7
Benchmark	No		Dynamic feed-forward	11.57	11.51	0.5
Benchmark	No		Pure PID	11.57	10.63	8.1
Dynamic ramping	No		Dynamic feed-forward	14.17	13.15	7.1
Dynamic ramping	No		Pure PID	14.17	13.51	4.6
Dynamic ramping	No		Static feed-forward	14.17	13.20	6.8

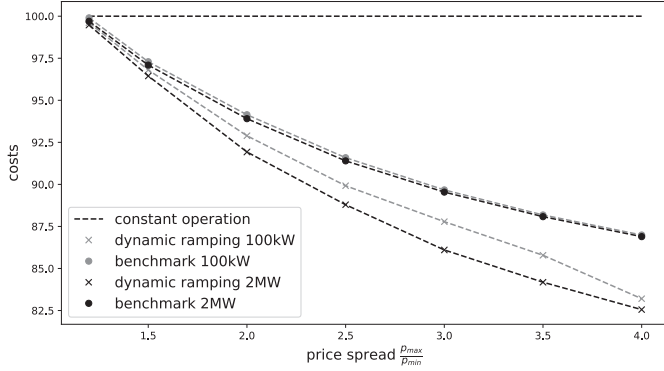


Fig. 13. Cost reduction in % relative to constant production, normalized over the electricity price spread p_{max} and minimum p_{min} . Simulation results compare dynamic ramping and benchmark methods for a 100 kW test bench and a 2 MW electrolyzer, considering differences in thermal mass and heat transfer. Larger electrolyzers with slower dynamics achieve greater cost savings with dynamic ramping.

$1.30 \cdot 10^7$ J/K and the heat transfer resistance from $R_{HT100kW} = 77.5$ W/K to $R_{HT2MW} = 847$ W/K.

Furthermore, we adapt our generic electricity price profile and maintain the staircase profile but vary the price spread between the maximum and minimum electricity price between 1.2 and 4.

As the 2 MW electrolyzer has slower dynamics, the improvement of the dynamic ramping method compared to the benchmark is higher compared to the 100 kW electrolyzer for every price spread, e.g., or a price spread of 2, the improvement is 2 % instead of 1 % (Fig. 13). Thus, our dynamic ramping approach might offer even higher cost reductions for electrolyzers with higher power.

6. Discussion on aging and overload

We performed our experiments within a few days, during which the characteristics of our electrolyzer remained roughly constant. However, over the course of the electrolysis cell's lifetime, substantial ageing takes place within it. This aging can be recognized by an increase in cell voltage. Here, we briefly discuss two known aging phenomena to obtain an overview: On the one hand, corrosion within the cell leads to aging effects. These corrosion phenomena are strongly related to high electrical potential on the anode side [47,48]. On the other hand, the aging mechanism depends on ionic contaminants, which poison the membrane and electrode layers. The origin of these ions is, e.g., metal bipolar plates, sealing gaskets, or feed water that enters the system [47,49]. With these degradation effects, the electric conductivity inside the cell decreases such that for a constant electrical current, the cell voltage increases. Fig. 4 in Section 2.2.1 has previously demonstrated the impact of aging on the cell voltage of the 100 kW PEM electrolyzer, showing a maximum increase of $\Delta U_{age} = 0.05$ V at high power densities. To address

these degradation effects, the model of U_{cell} presented in Eq. (4) was adapted using Eq. (6). The parameters a_1 and a_2 were applied to target U_{ohm} and η_{act} of U_{cell} , as these terms depend on material properties and therefore capture aging effects. However, a specific correlation between aging and the individual model parameters, such as the charge transfer coefficient, along with the associated aging processes, was not further pursued in this context. To ensure that the algorithm can accommodate aging effects, including an increase in cell voltage, the parameters a_1 and a_2 must be progressively adjusted over time.

To represent a time dependent value the progressive aging of the PEM stack is described as a cell voltage increase per hour of operation ($\mu V/h$). Values from 2.5 to 20 $\mu V/h$ can be found in the literature [49–51]. Such aging in PEM electrolysis has an effect on our algorithm. As the hydrogen produced is mainly dependent on the current density, this leads to the conclusion that the input power to the PEM electrolysis process increases for a given production rate. In other words, an increased input power is needed for the same output power, i.e., the efficiency of the electrolyzer decreases. Therefore, the existing electrolyzer must become warmer over the existing operating range due to the increased input power with the same output power. Eq. (7) from Section 2.2.3 outlines this relationship: If $\sum_k \dot{Q}_k$ increases, a temperature change is taking place. Consequently, this leads to an increased demand for cooling power during operation.

There are two ways to address aging in electrolyzers, visualized in Fig. 14: First, the cooling capacity of the electrolyzer can be initially designed to be higher. For our experiment, the maximum cooling power was determined to $\dot{Q}_{control}^{max} = 3.6$ kW, as represented by the blue curve in Fig. 14 (upper part). Utilizing this cooling capacity, the maximal possible power and temperature with our aging are $p_{max,steady} = 50.3$ kW and $T_{stack}^{max} = 80$ °C (compare to Section 2.3). However, with a voltage increase due to aging ΔU_{age} , the maximum steady-state power $p_{max,steady}$ constantly reduces. The orange curve in Fig. 14 (upper part) represents a higher cooling power of $\dot{Q}_{control}^{max} = 5.4$ kW for the same conditions, which initially leads to a higher possible power. With an aging of $\Delta U_{age} = 0.1$ V, the maximum feasible steady-state power is again $p_{max,steady} = 50.3$ kW. Thus, even with a higher cooling capacity the same maximum steady-state power is reached due to aging after a given amount of operating hours. With the given degradation rate of 2.5–20 $\mu V/h$, Fig. 14(lower part) illustrates the achievable operational hours under specified conditions. In our scenario, feasible operational durations range from 5.000 to 40.000 h until the maximum power output, $p_{max,steady} = 50.3$ kW, is attained. Overall, realizing a higher cooling power results in increased investment costs but has the advantage of allowing the electrolyzer to operate under higher power in steady state, even given progressive aging.

On the other hand, the cooling capacity can be designed to meet the initial cooling requirements of the electrolyzer $\dot{Q}_{control}^{max} = 3.6$ kW, shown in the blue curve in Fig. 14(upper part). This approach has lower investment costs. However, a primary disadvantage is that the algorithm's limits must be periodically adjusted to account for the decline in the maximum feasible steady-state power. Moreover, the periods of overload, which require higher cooling capacity, will be shorter.

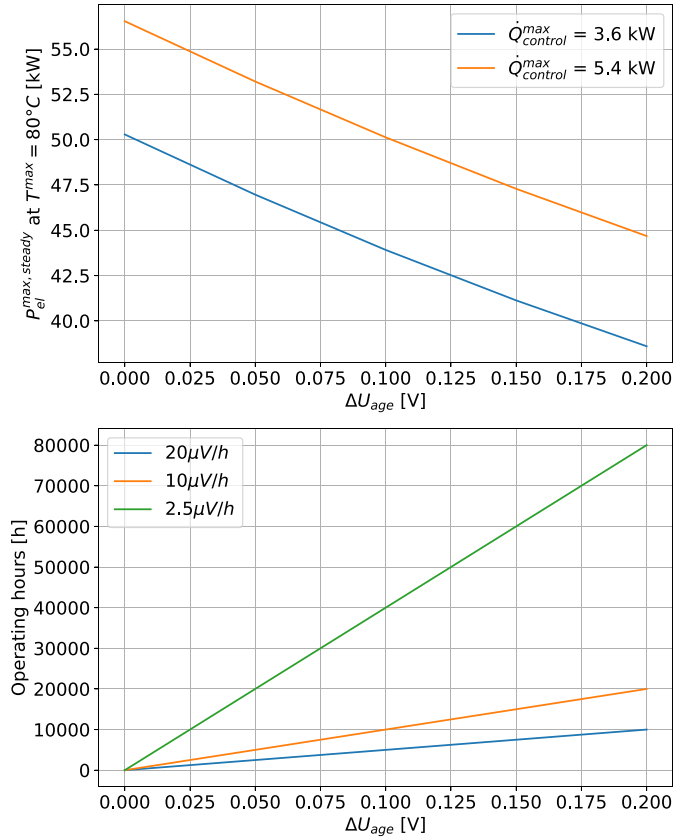


Fig. 14. Maximum steady-state-feasible power $P_{el}^{max,steady}$ at $T^{max} = 80$ °C as a function of voltage increase due to aging ΔU_{age} for different cooling powers $\dot{Q}_{control}^{max}$ (upper part). Corresponding operating hours for a given aging rate.

From an economic perspective, both options must be weighed against each other in order to make an informed assessment. However, this evaluation is challenging and cannot be generalized, as various factors, such as the extraction of thermal energy or accelerated aging, play significant roles in later applications. While the most effective approach cannot be conclusively determined within the scope of this work, the dynamic ramping limits can be successively adapted to the aged stack by updating the underlying electrolyzer model. Thus, if overload operation is promising in one period of the electrolyzer's lifetime, our dynamic ramping approach can be applied.

In addition to the possibility of adjusting the algorithm during the aging process, the question arises as to whether the existing overload operation accelerates degradation. With the developed dynamic ramping approach, electrolyzers are operated under overload conditions for a certain period of time. With a normal operation range of 0.5–2.5 A/cm² [52], overload conditions can be considered to occur at current densities exceeding 2.5 A/cm². This overload condition can result in an accelerated rate of cell degradation compared to nominal load conditions [49,52–54]. With respect to Section 1, various manufacturers, however, allow overload operation for a certain period of time. As stated previously, a time-dependent value for degradation is described as a cell voltage increase per hour of operation (μV/h). Eq. (20) defines the correlation between current density j_{el} and the degradation rate D_{rate} (μV/h), describing the functional dependence of degradation on the applied current density:

$$D_{rate} = f(j_{el}) \quad (20)$$

In [55], a PEM single cell with an active area of 30.624 cm² was evaluated at 80 °C under accelerated stress test conditions. The degradation

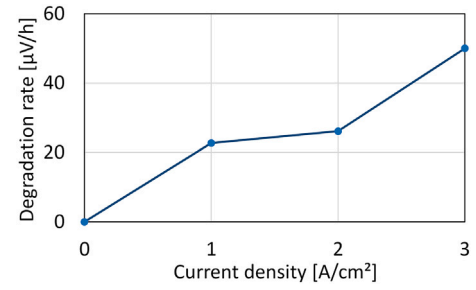


Fig. 15. Degradation rate μV/h depending on the current density A/cm² up to overload of 3 A/cm²; data derived from Su et al. [55].

rates at current densities of 1, 2, and 3 A/cm² were determined to be 22.7, 26.1, and 50 μV/h, respectively, over a 600-h operational period. This relationship is graphically depicted in Fig. 15.

In the used aging model [55], the degradation rate increases for current densities exceeding 2 A/cm². Based on this, we conducted an analysis of our dynamic ramping method to assess whether higher degradation rates occur or if operating under overload conditions for a certain period of time is permissible. For this, we analyzed two distinct scenarios. The first scenario used a current density trajectory of dynamic ramping and benchmark case without turn-off (Fig. 16(a)). The second scenario used a current density trajectory of dynamic ramping and benchmark case with turn-off (Fig. 16(b)). For these scenarios, the current density was adjusted to the range for overload conditions.

In Section 3.2.1 with Eq. (Pd), it was defined that the nominal hydrogen production $n_{H_2}^{nom}$ for each scenario has the same amount over the given time horizon $[t_0, t_f]$, to ensure the comparability of all results in relation to cost reduction. Based on Faraday's law, Eq. (8) in Section 2.2.3, the integral of the current density for the benchmark approach, j_{el-BM} , and the dynamic ramping approach, j_{el-DR} , must be equal to the nominal current density, j_{el}^{nom} , over a given time horizon $[t_0, t_f]$. This relationship is expressed in Eq. (21).

$$\int_{t_0}^{t_f} j_{el-BM}(t) dt = \int_{t_0}^{t_f} j_{el-DR}(t) dt = j_{el}^{nom}(t_f - t_0) \quad (21)$$

Applying these integrals to our two scenarios revealed the equality of the nominal current density j_{el}^{nom} in both methods, as illustrated in Fig. 16 by the dotted lines. The degradation derived from Fig. 15, along with the trajectories of the two scenarios from Fig. 16 was utilized to calculate the nominal degradation rate D_{rate}^{nom} over the defined time horizon $[t_0, t_f]$, as expressed in Eq. (22). This approach enabled a comparative analysis of the dynamic ramping and benchmark case in terms of degradation.

$$\int_{t_0}^{t_f} D_{rate}(j_{el}(t)) dt = D_{rate}^{nom}(t_f - t_0) \quad (22)$$

In Fig. 17, the degradation rates for both scenarios, related to the current densities, are illustrated. It can be directly seen that the nominal degradation rate D_{rate}^{nom} of the benchmark is slightly higher than the dynamic ramping method in both scenarios, indicated by the dotted lines.

Examining Table 4, it becomes evident that the nominal degradation rate of the benchmark approach with no turn-off is approximately 1 % higher. With turning off the current density, the nominal degradation rate of the benchmark approach is even higher at approximately 2 % compared to the dynamic ramping method.

That means in both scenarios—no turn-off and turn-off—a higher degradation rate is observed for the benchmark approach. A closer examination reveals a possible explanation: while the dynamic ramping method periodically operates at lower current densities, the benchmark approach remains at higher current densities for extended periods, leading to additional degradation. Overall, the nominal degradation rate

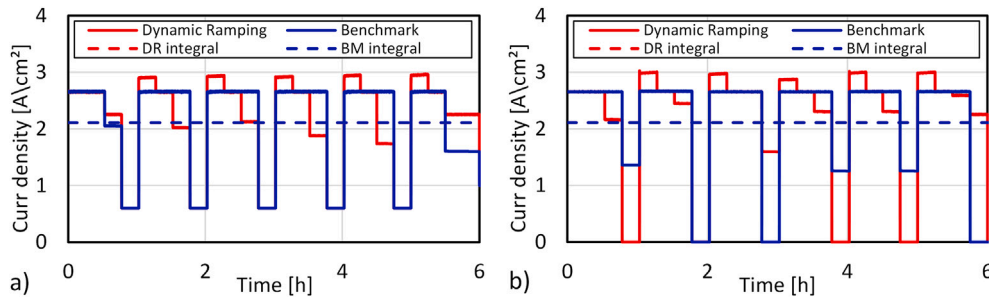


Fig. 16. (a) Trajectory current density of dynamic ramping and benchmark approach (no turn-off) and (b) Trajectory current density of dynamic ramping and benchmark approach (turn-off).

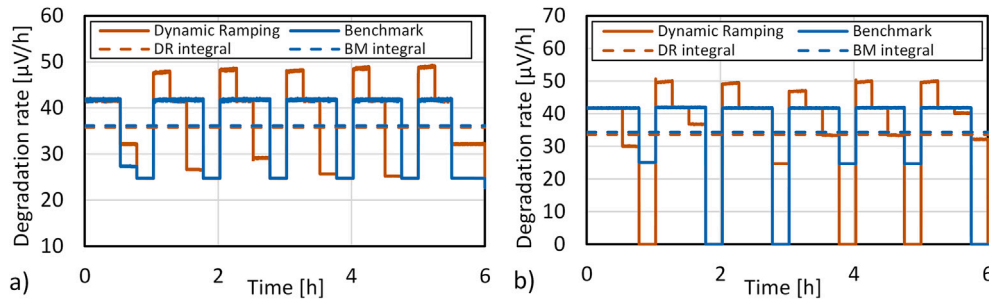


Fig. 17. (a) Trajectory degradation rate of dynamic ramping and benchmark (no turn-off); (b) trajectory degradation rate of dynamic ramping and benchmark (turn-off).

Table 4

Comparison of the nominal degradation rate D_{rate}^{nom} between Dynamic ramping and Benchmark approach for the two defined scenarios (compare to Fig. 17).

Scenario	D_{rate}^{nom} [μV/h]		Deviation [%]
	Dynamic ramping	Benchmark	
j_{el} Trajectory no turn-off	35.79	36.17	1.04
j_{el} Trajectory turn-off	33.64	34.32	2.03

behaves similarly for both approaches, indicating that no additional aging is expected due to operation under overload conditions for a certain period of time.

But nevertheless, not only the high current densities affect degradation. PEM electrolyzers normally operate in the temperature range of 50–80 °C [56,57]. If temperature gets too low, higher membrane resistances can arise, which can cause long-term thermal and electrochemical stress due to overpotential on the membrane [58,59]. However, temperatures above the defined range cause much more trouble because they increase the rate of electrochemical reactions, which leads to changes in the membrane, catalyst, and bipolar plates [57,58]. In our experiments, the PEM-Stack temperature consistently exceeds 55 °C, with minimum temperatures reaching approximately 60 °C when the load remains active. Additionally, in our experiments, the temperature never surpassed 80 °C. These conditions ensured that the system operated within the targeted temperature range, leading to the assumption that no significant aging effects would occur. However, not only do high and low stack temperatures have an influence, it is also important to consider that continuous temperature fluctuations may also influence the structural integrity and performance of key components, such as membrane materials and catalysts. Variations in operating temperature can induce mechanical stress, chemical degradation, or changes in reaction kinetics, potentially leading to reduced efficiency over time. These effects could also compromise the long-term stability of the system. As previously described, our method allows for an active modification of the

temperature trajectory, providing the capability to dynamically control the temperature if it deviates from the desired range. This demonstrates the robustness of our method against degradation and offers a more comprehensive analysis of electrolyzer performance under dynamic load conditions.

However, aging remains a subject of ongoing research, as not all degradation mechanisms are yet fully understood. In addition to ensure that the electrolyzer operates under optimal conditions to mitigate electrochemical, mechanical, and thermal stress, it is essential to pursue advancements in material science aimed at improving membrane and catalyst properties. Furthermore, operational parameters can be dynamically adjusted in response to aging through the implementation of predictive operating strategies and advanced control mechanisms. This remains a critical challenge for the large-scale commercialization of PEM electrolysis and represents a key area requiring further research and development. Nevertheless, we emphasize that we employed a literature-based model, and the observed aging was even lower than expected.

7. Conclusions

Through the use of renewable energy sources such as wind power and solar photovoltaics, fluctuating electricity prices are expected, which makes demand response through flexible production promising for electrolyzers. Our results experimentally demonstrate that the dynamic ramping concept increases flexibility through overload operation for electrolyzers with slow temperature dynamics. The experiments highlighted a notable 3.8 % reduction in costs compared to the benchmark without overload operation. At the same time, the PEM electrolyzer model exhibits only a 0.6 % deviation in costs from the experimental results, and the needed cooling power was only slightly overestimated.

The employed two-layer approach with scheduling and control allows the rejection of non-modeled disturbances and tracks the scheduled temperature profile well. In the control layer, a feed-forward scheme was found to be advantageous compared to a pure tracking control when the electric current performs a step change.

Expanding our simulations to a 2 MW scale electrolyzer revealed even greater cost reductions with the dynamic ramping method, owing to the slower dynamics of the larger electrolyzer. Consequently, our dynamic ramping approach promises to reduce costs through demand response, particularly for electrolyzers with higher power capacities.

The main contributions of this publication lie in the experimental validation of the dynamic ramping approach and the development and experimental validation of suitable feed-forward controllers. Moreover, we discuss potential degradation effects due to overload and flexible temperature conditions. The dynamic ramping and benchmark approaches show similar nominal degradation rates, with no major increase under short-term overloads. Notably, dynamic ramping offers a slight benefit by reducing overload-induced aging, enhancing overall system resilience. In case of flexible temperature conditions our experiments ensured operation within the optimal 55–80 °C range, minimizing aging effects. Furthermore, our method allows for active stack temperature control, further enhancing system stability and reliability. In addition, we demonstrate and discuss the necessary adaptations of the underlying model to aging, which cannot be totally avoided for PEM-electrolyzers. However, the mechanisms driving aging in PEM electrolyzers remain the focus of ongoing and in-depth scientific research.

CRedit authorship contribution statement

Roger Keller: Writing – original draft, Visualization, Validation, Investigation, Formal analysis, Data curation. **Florian Joseph Baader:** Writing – review & editing, Writing – original draft, Visualization, Software, Resources, Methodology, Investigation, Formal analysis, Conceptualization. **André Bardow:** Writing – review & editing. **Ralf Peters:** Writing – review & editing.

Declaration of competing interest

The authors declare that they have no known competing financial interests or personal relationships that could have appeared to influence the work reported in this paper.

Acknowledgments

F.B. and A.B. acknowledge funding by the Swiss Federal Office of Energy's SWEET program as part of the project PATHFNR.

Appendix

Dynamic ramping constraints for electrolyzers

In this section, we summarize the reformulation of dynamic ramping constraints for electrolyzers in accordance with our previous publication [31,32]. For electrolyzers with slow temperature dynamics, the reformulation is based on a few assumptions regarding the model's structure, which are typically true (e.g., compare to [22,30,60,61]) and also hold for our test bench model, which reasonably models the operation. These structural assumptions are visualized on the left-hand side of Fig. 18. We assume that the system has two degrees of freedom: the electric current density j_{el} and a cooling input; $\dot{Q}_{control}$ in our case. Note that we hold the pressures p_{H_2} , p_{O_2} constant during operation. Furthermore, we assume that the temperature dynamics are the only dynamics slow enough to be relevant on the scheduling-relevant time scale typically dictated by energy price intervals, e.g., 1 h or 15 min. Thus, the temperature T_{Stack} is the only differential state of the model, where the time derivative \dot{T}_{Stack} is a nonlinear function of the two inputs and the current temperature:

$$\dot{T}_{Stack} = f(T_{Stack}, j_{el}, \dot{Q}_{control}) \quad (23)$$

The other two scheduling-relevant model outputs are the product flow of hydrogen \dot{n}_{H_2} , and the electric input power P_{el} , which essentially dictates the electricity costs.

Table 5
Model parameters.

	Value	Unit	Interpretation
N_{cell}	54	cm ²	Active cell surface
A_{cell}	300	–	Number of cells
F	96.485	As/mol	Faraday constant
a_1	0.995	–	Empiric parameter
R_{mem}	0.120	Ω	Membrane resistance
R_{con}	0.096	Ω	Membrane resistance
R_{gas}	8.314	J/mol K	Gas constant
j_0	0.00000012	A/cm ²	Exchange current density
α	0.024	V	Charge transfer coefficient
M_{H_2O}	18.015	g/mol	Molar mass water
d_1	–0.044	kJ/mol K	Vaporization slope (0..100 °C)
d_2	57.07	kJ/mol	Vaporization constant (0..100 °C)
D	1.9	mol/mol H ⁺	Drag factor
$\Delta H_{H_2, H_2}$	20	J/mol	Higher heating value hydrogen
$R_{HT100kW}$	77.5	W/K	Heat transfer resistance 100 kW electrolyzer
R_{HT2MW}	847	W/K	Heat transfer resistance 2 MW electrolyzer
T_{surr}	25	°C	Surrounding temperature
C_{100kW}	$3.00 \cdot 10^5$	J/K	Thermal mass 100 kW electrolyzer
C_{2MW}	$1.30 \cdot 10^7$	J/K	Thermal mass 2 MW electrolyzer

Table 6
Specification stack 100 kW PEM electrolyzer.

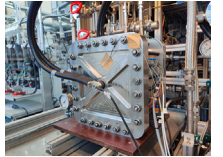
Specification	Value	Unit	Stack image
Number cells	27		
Maximal power	6	W/cm ²	
Coating cathode side	Platinum 0.940	mg/cm ²	
Coating anode side	Iridium 2.610	mg/cm ²	
Membrane	Nafion 117		
Cell area	300	cm ²	
Bipolar plates	Metal		

Table 7
Operating conditions 100 kW PEM electrolyzer.

Specification	Value	Unit
Cell voltage	U_{cell}	0..2 V
Current density	j_{el}	0..3 A/cm ²
Pressure anode	p_{O_2}	0..50 bar
Pressure cathode	p_{H_2}	0..50 bar
Temperature	T_{Stack}	20..85 °C
Specific volume flow anode	\dot{V}_{anode}	0..10 ml/min cm ²
Specific volume flow cathode	$\dot{V}_{cathode}$	0..10 ml/min cm ²

Table 8
Parameter adaptive PID control.

Operation condition	K_C	T_N (min)	T_V (min)
$0 < j_{el} \leq 0.5 \text{ A/cm}^2 \wedge 75^\circ\text{C} < T_{Stack}$	65.78	87.71	0.84
$0.5 < j_{el} \leq 1 \text{ A/cm}^2 \wedge 75^\circ\text{C} < T_{Stack}$	52.63	87.71	0.84
$1 < j_{el} \leq 1.5 \text{ A/cm}^2 \wedge 75^\circ\text{C} < T_{Stack}$	35.08	87.71	0.84
$1.5 < j_{el} \text{ A/cm}^2 \wedge 75^\circ\text{C} < T_{Stack}$	25.06	87.71	1.26

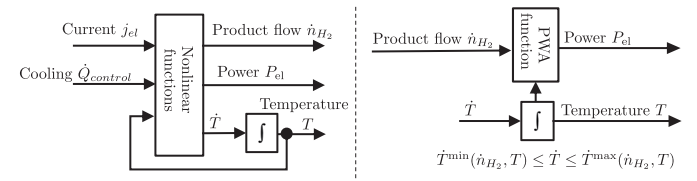


Fig. 18. Original nonlinear model (left) and reformulation with piecewise affine (PWA) function and dynamic ramping constraint (right).

The concept of dynamic ramping constraints is to use scheduling-relevant outputs for hydrogen production \dot{n}_{H_2} and temperature-derivative \dot{T}_{Stack} as degrees of freedom during the scheduling optimization (right-hand part of Fig. 18). This change in the degrees of freedom is possible because of the underlying control layer: If scheduling passes feasible trajectories for the outputs \dot{n}_{H_2} , \dot{T}_{Stack} as set-points, the underlying control can choose the physical inputs j_{el} , $\dot{Q}_{control}$ to realize the set-point trajectories. However, the control inputs j_{el} , $\dot{Q}_{control}$ have upper and lower bounds, which cannot be enforced in a straightforward way to the reformulated model, as these variables are not present anymore (right-hand part of Fig. 18). For the current density j_{el} , this issue can still be resolved rigorously as the hydrogen production \dot{n}_{H_2} is proportional to the current density j_{el} and so the limits of the current density j_{el} can be translated into limits on the hydrogen production \dot{n}_{H_2} . However,

the cooling power $\dot{Q}_{control}$ does not translate linearly to the temperature derivative \dot{T}_{Stack} and, additionally, depends on the current density j_{el} (or hydrogen production \dot{n}_{H_2}) and temperature T_{Stack} . Thus, the upper and lower bound of $\dot{Q}_{control}$ convert into minimum and maximum temperature derivatives \dot{T}_{Stack}^{min} , \dot{T}_{Stack}^{max} , which are nonlinear functions of production and temperature:

$$\dot{T}_{Stack}^{min}(\dot{n}_{H_2}, T_{Stack}) \leq \dot{T}_{Stack} \leq \dot{T}_{Stack}^{max}(\dot{n}_{H_2}, T_{Stack}) \quad (24)$$

As these functions \dot{T}_{Stack}^{min} , \dot{T}_{Stack}^{max} limit how fast the temperature can be ramped, they are called dynamic ramping limits.

The dynamic ramping limits for our test bench are shown in Fig. 19(a). To model these nonlinear constraints by a PWA approximation, we chose ten PWA segments in \dot{n}_{H_2} (Fig. 19(b)). As in previous work [31,32], we approximate the ramping limits as being linear with

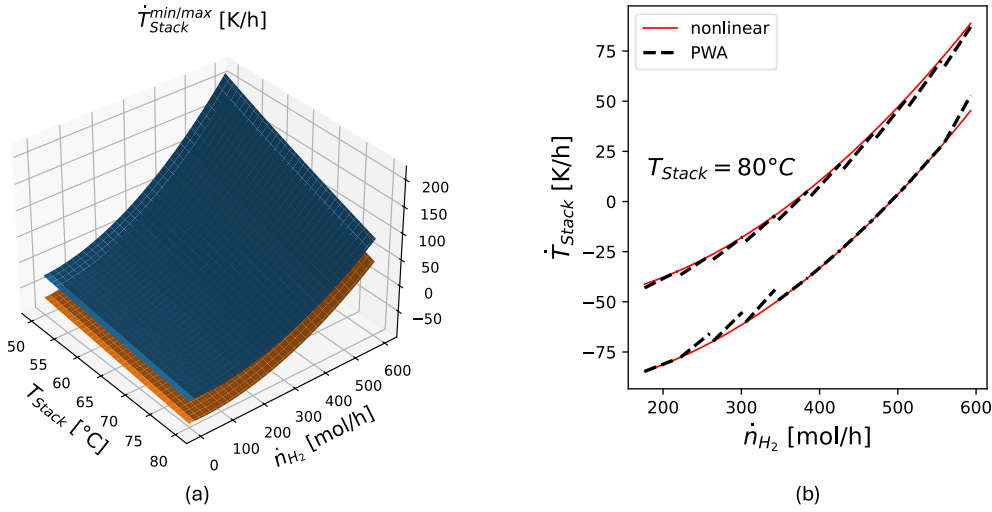


Fig. 19. Dynamic ramping limits for the analyzed electrolyzer: (a) Minimum achievable temperature derivative \dot{T}_{Stack}^{min} and maximum achievable temperature derivative \dot{T}_{Stack}^{max} as a function of temperature T_{Stack} and hydrogen production rate \dot{n}_{H_2} . (b) Comparison of nonlinear dynamic ramping limits and PWA approximation for a temperature T_{Stack} of 80 °C.

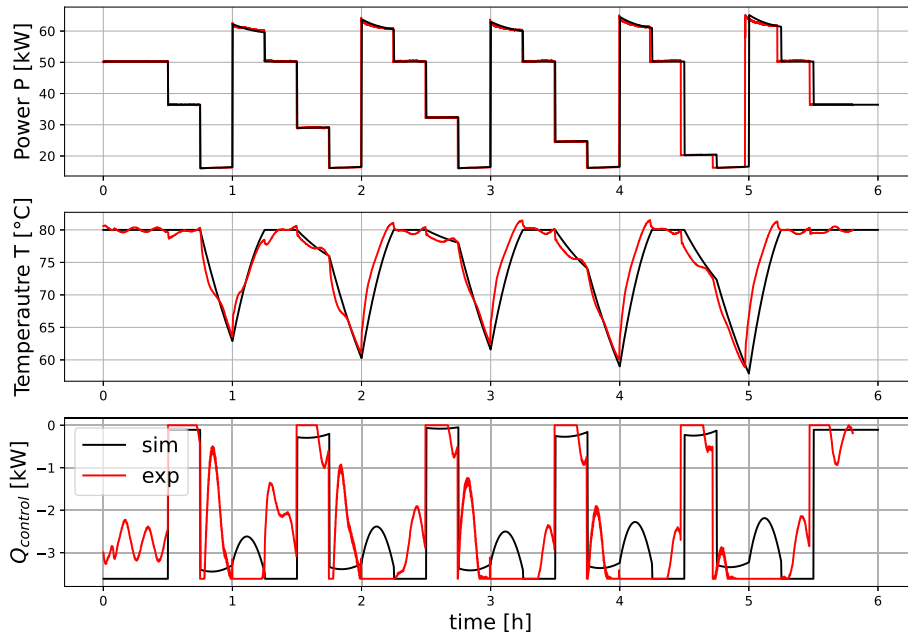


Fig. 20. Evaluation of the dynamic feed-forward control scheme comparing power, temperature, and cooling power $\dot{Q}_{control}$ between simulation (sim) and experiment (exp.). The case comprises dynamic ramping without turn off (Experiment $DR_{DFF}^{no\ off}$ in Table 1).

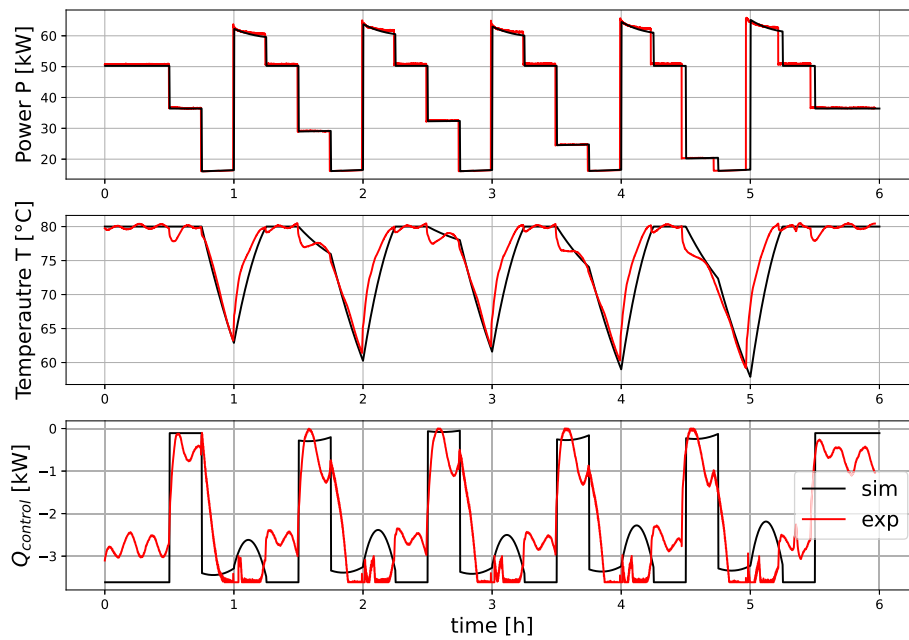


Fig. 21. Evaluation without a feed-forward control scheme comparing power, temperature, and cooling power $\dot{Q}_{control}$ between simulation (sim) and experiment (exp.). The case comprises dynamic ramping without turn off (Experiment $DR_{PID}^{no\ off}$ in Table 1).

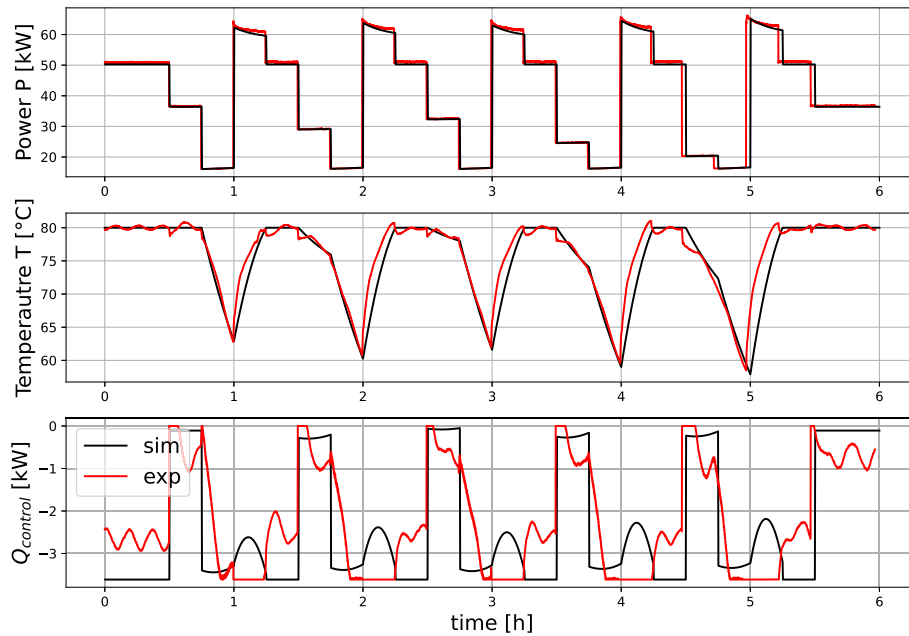


Fig. 22. Evaluation of the static feed-forward control scheme comparing power, temperature, and cooling power $\dot{Q}_{control}$ between simulation (sim) and experiment (exp.). The case comprises dynamic ramping without turn off (Experiment $DR_{SFF}^{no\ off}$ in Table 1).

the temperature T_{Stack} , as the temperature dependency is mostly given by convective temperature losses to the ambient, which can be assumed to be proportional to the difference between the electrolyzer and ambient temperature. In principle, many multi-variate regression methods, e.g., hinging hyperplanes [62–64], convex region surrogates [65,66], or artificial neural networks with ReLU activation functions [67,68] could be used here to find PWA approximations.

Data availability

Data will be made available on request.

References

- [1] Hu S, et al. A comprehensive review of alkaline water electrolysis mathematical modeling. *Appl Energy* 2022;327:120099.
- [2] Guo Y, Li G, Zhou J, Liu Y. Comparison between hydrogen production by alkaline water electrolysis and hydrogen production by PEM electrolysis. *IOP Conf Ser Earth Environ Sci* 2019;371:042022.
- [3] Matute G, Yusta J, Correas L. Techno-economic modelling of water electrolyzers in the range of several MW to provide grid services while generating hydrogen for different applications: a case study in Spain applied to mobility with fcevs. *Int J Hydrog Energy* 2019;44:17431–42.
- [4] Keller R, Rauls E, Hehemann M, Müller M, Carmo M. An adaptive model-based feedforward temperature control of a 100 kW PEM electrolyzer. *Control Eng Pract* 2022;120:104992.

- [5] Burre J, Bongartz D, Brée L, Roh K, Mitsos A. Power-to-X: between electricity storage, e-production, and demand side management. *Chem Ing Tech* 2020;92:74–84.
- [6] Esche E, Repke J-U. Dynamic process operation under demand response – a review of methods and tools. *Chem Ing Tech* 2020;92:1898–909.
- [7] Qi R, et al. Thermal modeling and controller design of an alkaline electrolysis system under dynamic operating conditions. *Appl Energy* 2023;332:120551.
- [8] Fischer D, Kaufmann F, Hollinger R, Voglstätter C. Real live demonstration of MPC for a power-to-gas plant. *Appl Energy* 2018;228:833–42.
- [9] Serna Á, Yahyaoui I, Normey-Rico J, de Prada C, Tadeo F. Predictive control for hydrogen production by electrolysis in an offshore platform using renewable energies. *Int J Hydrog Energy* 2017;42:12865–76.
- [10] Zhou Z, Unsworth P, Holland P, Igc P. Design and analysis of a feedforward control scheme for a three-phase voltage source pulse width modulation rectifier using sensorless load current signal. *IET Power Electron* 2009;2:421–30.
- [11] Liu B, Song Z, Yu B, Yang G, Liu J. A feedforward control-based power decoupling strategy for grid-forming grid-connected inverters. *Energies* 2024;17:424.
- [12] Azwar M, Hussain M, Wahab A, Zamil M. A comparative study between neural networks (NN)-based and adaptive-pid controllers for the optimal bio-hydrogen gas production in microbial electrolysis cell reactor. *Comput Aided Chem Eng* 2015;37:1529–34.
- [13] Conker C, Baltacıoglu M. Fuzzy self-adaptive pid control technique for driving HHO dry cell systems. *Int J Hydrog Energy* 2020;45:26059–69.
- [14] Scheepers F, et al. Temperature optimization for improving polymer electrolyte membrane-water electrolysis system efficiency. *Appl Energy* 2021;283:116270.
- [15] Scheepers F, Stähler M, Stähler A, Müller M, Lehnert W. Cost-optimized design point and operating strategy of polymer electrolyte membrane electrolyzers. *Int J Hydrog Energy* 2023;48:112185 – 12199.
- [16] Vives AM, Wang R, Roy S, Smallbone A. Techno-economic analysis of large-scale green hydrogen production and storage. *Appl Energy* 2023;346:121333.
- [17] Zhu Q, et al. Optimizing efficiency of proton exchange membrane electrolyzer system based on multiphysics model and differential evolution strategy. *J Power Sources* 2024;621:235270.
- [18] Zhang H, Yuan T. Optimization and economic evaluation of a PEM electrolysis system considering its degradation in variable-power operations. *Appl Energy* 2022;324:119760.
- [19] Henry A, McStay D, Rooney D, Robertson P, Foley A. Techno-economic analysis to identify the optimal conditions for green hydrogen production. *Energy Conv Manag* 2023;291:117230.
- [20] Nasser M, Hassan H. Techno-enviro-economic analysis of hydrogen production via low and high temperature electrolyzers powered by PV/wind turbines/waste heat. *Energy Conv Manag* 2023;278:116693.
- [21] Fabianek P, Madlener R. Techno-economic analysis and optimal sizing of hybrid PV-wind systems for hydrogen production by PEM electrolysis in California and Northern Germany. *Int J Hydrog Energy* 2024;67:1157–72.
- [22] Gabrielli P, et al. Modeling for optimal operation of PEM fuel cells and electrolyzers. In: 2016 IEEE 16th international conference on environment and electrical engineering (EEEIC); 2016. p. 1–7.
- [23] Buttler A, Spliethoff H. Current status of water electrolysis for energy storage, grid balancing and sector coupling via power-to-gas and power-to-liquids: a review. *Renew Sustain Energy Rev* 2018;82:2440–54.
- [24] Flamm B, Peter C, Büchi F, Lygeros J. Electrolyzer modeling and real-time control for optimized production of hydrogen gas. *Appl Energy* 2021;281:116031.
- [25] Kopp M, et al. Energiepark Mainz: technical and economic analysis of the world-wide largest power-to-gas plant with PEM electrolysis. *Int J Hydrog Energy* 2017;42:13311–20.
- [26] Simkoff J, Baldea M. Stochastic scheduling and control using data-driven nonlinear dynamic models: application to demand response operation of a chlor-alkali plant. *Ind Eng Chem Res* 2020;59:21.
- [27] Kopp M. Strommarktseitige Optimierung des Betriebs einer PEM-Elektrolyseanlage [Ph.D. thesis]. Kassel: Universität Kassel; 2018.
- [28] Ulleberg Ø. Modeling of advanced alkaline electrolyzers: a system simulation approach. *Int J Hydrog Energy* 2003;28:21–33.
- [29] Otashu J, Baldea M. Demand response-oriented dynamic modeling and operational optimization of membrane-based chlor-alkali plants. *Comput Chem Eng* 2019;121:396–408.
- [30] Ulleberg Ø. Stand-alone power systems for the future: optimal design, operation and control of solar [Ph.D. thesis]. Trondheim: Norwegian University of Science and Technology; 1998.
- [31] Baader F, Bardow A, Dahmen M. Milp formulation for dynamic demand response of electrolyzers. In Yamashita Y, Kano M, editors. 14th International symposium on process systems engineering, vol. 49 of computer aided chemical engineering. Elsevier; 2022. p. 391–6.
- [32] Baader F. Simultaneous real-time scheduling of multi-energy systems and dynamic production processes [Ph.D. thesis]. RWTH Aachen University; 2023. <https://publications.rwth-aachen.de/record/962430>
- [33] Fliess M, Lévine J, Martin P, Rouchon P. Flatness and defect of non-linear systems: introductory theory and examples. *Int J Control* 1995;61:13–27.
- [34] Baader F, Althaus P, Bardow A, Dahmen M. Demand response for flat nonlinear mimo processes using dynamic ramping constraints. *Comput Chem Eng* 2023;172:108171.
- [35] Tjarks G. PEM-Elektrolyse-Systeme zur Anwendung in Power-to-Gas Anlagen [Ph.D. thesis], RWTH Aachen University; 2017. <https://publications.rwth-aachen.de/record/689617>
- [36] Huang P. Humidity standard of compressed hydrogen for fuel cell technology. *ECS Trans* 2008;12:479–84.
- [37] Harjunkoski I, Nyström R, Horch A. Integration of scheduling and control—theory or practice? *Comput Chem Eng* 2009;33:1909–18.
- [38] Engell S, Harjunkoski I. Optimal operation: scheduling, advanced control and their integration. *Comput Chem Eng* 2012;47:121–33.
- [39] Baldea M, Harjunkoski I. Integrated production scheduling and process control: a systematic review. *Comput Chem Eng* 2014;71:377–90.
- [40] Ellis M, Durand H, Christofides P. A tutorial review of economic model predictive control methods. *J Process Control* 2014;24:1156–78.
- [41] Zhang Q, Grossmann I. Planning and scheduling for industrial demand side management: advances and challenges. In Martín M, editor. *Alternative energy sources and technologies, engineering*. Switzerland: Springer; 2016. p. 383–414.
- [42] Biegler L. *Nonlinear programming: concepts, algorithms, and applications to chemical processes*. Philadelphia, USA: Society for Industrial and Applied Mathematics; 2010.
- [43] Nicholson B, Sirola J, Watson J-P, Zavala V, Biegler L. Pyomo.Dae: a modeling and automatic discretization framework for optimization with differential and algebraic equations. *Math Program Comput* 2018;10:187–223.
- [44] Gurobi Optimization, LLC. Gurobi optimizer reference manual; 2024. <http://www.gurobi.com> [Accessed 1 May 2024].
- [45] Rauls E, et al. Favorable start-up behavior of polymer electrolyte membrane water electrolyzers. *Appl Energy* 2023;330:120350.
- [46] Schäfer P, Daun T, Mitsos A. Do investments in flexibility enhance sustainability? A simulative study considering the German electricity sector. *AIChE J* 2020;66:e17010.
- [47] Wallnofer-Ogris E, Poimer F, Koll R, Macherhammer M-G, Trattner A. Main degradation mechanisms of polymer electrolyte membrane fuel cell stacks - mechanisms, influencing factors, consequences, and mitigation strategies. *Int J Hydrog Energy* 2024;50:1159–82.
- [48] Prestat M. Corrosion of structural components of proton exchange membrane water electrolyzer anodes: a review. *J Power Sources* 2023;556:232469.
- [49] Rakousky C, et al. Olymer electrolyte membrane water electrolysis: restraining degradation in the presence of fluctuating power. *J Power Sources* 2017;342:38–47.
- [50] Papakonstantinou G, et al. Degradation study of a proton exchange membrane water electrolyzer under dynamic operation conditions. *Appl Energy* 2020;280:115911.
- [51] Pantò F, Siracusano S, Briguglio N, Aricò A. Durability of a recombination catalyst-based membrane-electrode assembly for electrolysis operation at high current density. *Appl Energy* 2020;279:115809.
- [52] Voronova A, et al. Systematic degradation analysis in renewable energy-powered proton exchange membrane water electrolysis. *Energy Environ Sci* 2023;16:5170.
- [53] Ge X, et al. Early-stage performance degradation mechanisms of proton-exchange membrane water electrolysis under high operating current densities. *Fuel* 2025;386:134344.
- [54] Suermann M, Bensmann B, Hanke-Rauschenbach R. Degradation of proton exchange membrane (PEM) water electrolysis cells: looking beyond the cell voltage increase. *J Electrochem Soc* 2019;166:F645–52.
- [55] Su Z, Liu J, Li P, Liang C. Study of the durability of membrane electrode assemblies in various accelerated stress tests for proton-exchange membrane water electrolysis. *Materials* 2024;17:1331.
- [56] Schmidt O, et al. Future cost and performance of water electrolysis: an expert elicitation study. *Int J Hydrog Energy* 2017;42:30470–92.
- [57] Bonanno M, et al. Review and prospects of PEM water electrolysis at elevated temperature operation. *Adv Mater Technol* 2023;9:202300281.
- [58] Wallnofer-Ogris E, et al. A review on understanding and identifying degradation mechanisms in PEM water electrolysis cells: insights for stack application, development, and research. *Int J Hydrog Energy* 2024;65:381–97.
- [59] Tsotridis G, A. P. EU harmonised protocols for testing of low temperature water electrolyzers. Luxembourg, London, UK: Publications Office of the European Union; 2021.
- [60] Wang X, Tong C, Palazoglu A, El-Farra N. Energy management for the chlor-alkali process with hybrid renewable energy generation using receding horizon optimization. In: 53rd IEEE conference on decision and control; 2014. p. 4838–43.
- [61] Weigert J, Hoffmann C, Esche E, Fischer P, Repke J-U. Towards demand-side management of the chlor-alkali electrolysis: dynamic modeling and model validation. *Comput Chem Eng* 2021;149:107287.
- [62] Breiman L. Hinging hyperplanes for regression, classification, and function approximation. *IEEE Trans Inf Theory* 1993;39:999–1013.
- [63] Adeniran A, Ferik S. Modeling and identification of nonlinear systems: a review of the multimodel approach—part 1. *IEEE Trans Syst Man Cybern Syst* 2017;47:1149–59.
- [64] Kämper A, Holtwerth A, Leenders L, Bardow A. AutoMoG3D: automated data-driven model generation of multi-energy systems using hinging hyperplanes. *Front Energy Res* 2021;9:430.
- [65] Zhang Q, Grossmann I, Sundaramoorthy A, Pinto J. Data-driven construction of convex region surrogate models. *Optim Eng* 2016;17:289–332.
- [66] Schweidtmann A, Weber J, Wende C, Netze L, Mitsos A. Obey validity limits of data-driven models through topological data analysis and one-class classification. *Optim Eng* 2021;23:855–76.
- [67] Grimstad B, Andersson H. ReLU networks as surrogate models in mixed-integer linear programs. *Comput Chem Eng* 2019;131:106580.
- [68] Lueg L, Grimstad B, Mitsos A, Schweidtmann A. reluMIP: open source tool for MILP optimization of ReLU neural networks (v1.0.0); 2021. <https://zenodo.org/record/5601907?ylfhvt9csuk> [Accessed 14 April 2022].